HOMOGENIZATION-BASED MICROSCOPIC TEXTURE DESIGN AND OPTIMIZATION IN HYDRODYNAMIC LUBRICATION

A THESIS SUBMITTED TO
THE GRADUATE SCHOOL OF ENGINEERING AND SCIENCE
OF BILKENT UNIVERSITY
IN PARTIAL FULFILLMENT OF THE REQUIREMENTS FOR
THE DEGREE OF
MASTER OF SCIENCE
IN
MECHANICAL ENGINEERING

By
Abdullah Waseem
August 2016

HOMOGENIZATION-BASED MICROSCOPIC TEXTURE DESIGN AND OPTIMIZATION IN HYDRODYNAMIC LUBRICATION

By Abdullah Waseem

August 2016

We certify that we have read this thesis and that in our opinion it is fully adequate, in scope and in quality, as a thesis for the degree of Master of Science.

İlker Temizer (Advisor)

Yegan Erdem

Serdar Göktepe

Approved for the Graduate School of Engineering and Science:

Levent Onural
Director of the Graduate School

ABSTRACT

HOMOGENIZATION-BASED MICROSCOPIC TEXTURE DESIGN AND OPTIMIZATION IN HYDRODYNAMIC LUBRICATION

Abdullah Waseem
M.S. in Mechanical Engineering
Advisor: İlker Temizer
August 2016

The aim of this thesis is to develop an optimization framework for the texture optimization in hydrodynamic lubrication using multi-scale homogenization technique. In hydrodynamic lubrication the asperities do not come into contact due to fluid film present between the surfaces and normal load is carried by the viscous fluid. The Reynolds equation can be used with confidence for such problems. For two-scale separation, a basis for optimizing the surface textures is established through an asymptotic expansion based homogenization scheme, which delivers a macroscopic Reynolds equation containing homogenized coefficients. These homogenized coefficients depend on the fluid film thickness directly and by controlling these coefficients a desired macroscopic response can be obtained. Design variables are introduced to control the fluid film thickness indirectly through an intermediate filtering stage. Both microscopic and macroscopic objectives are defined for texture optimization. The quality of the designed textures are evaluated numerically as well as aesthetically and optimization parameters are selected accordingly. Isotropic and anisotropic textures can be designed by using the proposed optimization scheme. For both microscopic and macroscopic objectives optimization surface textures are reconstructed as a sanity check. Texture optimization for prescribed load bearing capacity and maximum load bearing capacity in temporal and spatial variations are then carried out for squeeze film flow and wedge problem, respectively. Finally, to reduce the computational cost, Taylor's expansion is proposed for the optimization problem. Overall, the methodology developed in this thesis froms a basis for a comprehensive micro-texture design framework for computational tribology.

Keywords: hydrodynamic lubrication, Reynolds equation, homogenization, texture design, multiscale interface mechanics.

ÖZET

HİDRODİNAMİK YAĞLAMADA TÜRDEŞLEŞTİRME TABANLI MİKROSKOPİK DESEN TASARIMI VE ENİYİLEMESİ

Abdullah Waseem
Makine Mühendisliği, Yüksek Lisans
Tez Danışmanı: İlker Temizer
Ağustos 2016

Bu tezin amacı, hidrodinamik yağlama problemleri için çok-ölçekli türdeşleştirme tekniklerine dayalı bir mikro-desen eniyileme çerçevesi geliştirmektir. Hidrodinamik yağlamada, arayüzeydeki sıvı tabakası nedeniyle pürüzlü yüzeyler birbirleriyle temas etmez, arayüzey yükü tamamıyla sıvı tarafından taşınır. Bu tip problemlerde Reynolds denklemi güvenilir şekilde kullanılabilir. Ölçekler ayrımı gözetildiğinde, yüzey desen eniyilemesinin temeli asimtotik açılım üzerine kurulabilir, ki bu yaklaşım ile içerisinde türdeşleştirilmiş katsayılar bulunan bir makro-denklem elde edilir. Türdeşleştirilmiş katsayıları yüzey deseni ile kontrol ederek istenilen bir makro-çözüme yaklaşmak mümkündür. Yüzey deseni filtrelemeye tabi tutulan tasarım değişkenleri vasıtasıyla betimlenmiştir. Hem mikroskopik hem de makroskopik hedefler ile elde edilen izotropik ve anizotropik mikro-desenler sayısal ve estetik özellikleriyle değerlendirilmiş, geniş bir problem yelpazesinde uygulanabilir eniyileme algoritması değişkenleri belirlenmiştir. Hesapsal çerçeve desen yeniden yapılandırılması ile kontrol edildiği gibi, arayüzeyin yük taşıma kapasitesinin eniyilemesine yönelik olan ve uzay-zaman içinde film kalınlığı değişimi içeren film sıkıştırma ve kama geometrisi gibi geleneksel problemlere de uygulanmıştır. Son olarak, hesapsal yükü azaltmak adına, eniyileme-türdeşleştirme bağının Taylor açılımı temelli kurulumu sınanmıştır. Genel olarak, bu tezde geliştirilen yaklaşım hesaplamalı tribolojide kapsamlı desen tasarımına yönelik bir temel oluşturmaktadır.

Anahtar sözcükler: hidrodinamik yağlama, Reynolds denklemi, türdeşleştirme, desen tasarımı, çok-ölçekli arayüzey mekaniği.

Acknowledgement

First and foremost, I am sincerely thankful to my mentor and thesis supervisor Dr. İlker Temizer. I appreciate his intelligence, passion for research work and firm grasp on the field of computational mechanics. Surely, without his continuous guidance and never ending support this research work would not have been completed. I also want to thank to our research collaborators Dr. Junji Kato and Dr. Kenjiro Terada from Tohoku University for their valuable advices on the optimization algorithm.

I would like show my gratitude to all the brilliant faculty members of the Department of Mechanical Engineering at Bilkent University, especially to Prof. Adnan Akay who always encouraged the department students to learn and help each other in research work and studies. I also thank Ms. Ela Özsoy for taking the time to help me whenever I had an administrative issue. It was my honor to be a part of such a bright and hard working department.

I must acknowledge all of my friends who were always there for me in my ups and downs and made my stay in Turkey memorable. It is my pleasure to mention some of the names here: Adeel Shahryar, Shahid Mehmood, Furqan Ali, Asad Ali, Nurulhude Baykal, Deepak Kumar Singh, Yahya Fikry, Alican Özkan, Buğra Türeyen, Serhat Kerimoğlu, Mümtazcan Karagöz, Alper Tiftikçi, Anıl Alan and Çağatay Karakan.

Most importantly, I thank my parents and siblings for their love and understanding, especially my mother Mrs. Javeria Waseem and my father Mr. Waseem Ahmed.

I also like to thank TÜBİTAK for financially supporting this research work under 1001 Programme (Grant No. 114M406).

Finally, I want to say: *Türkiye'm her şey için çok teşekkür ederim!*

Contents

List of Figures

List of Tables

Chapter 1

Introduction

This thesis deals with the optimization of micro-textures for hydrodynamic lubrication interfaces using Reynolds equation, with particular application to load capacity maximization in classical lubrication problems such as in squeeze film flow or fluid film bearing. The idea is to use the already developed optimization tools from different areas of science and apply these techniques to lubrication theory. The two-scale homogenization approach is implemented to separate the microscale from the macroscale. The microscale is then solely optimized for the desired macroscopic responses.

The idea of optimization in engineering problems can be found as early as in 1904 when Michell [1] came up with an economically distributed material for the structures carrying point loads. These so-called Michell-like structures are still being used as a benchmark problem in optimization of structures. With the advent of computational power and development of efficient numerical methods to solve challenging engineering problems, the structural optimization leaped in recent past with the introduction of optimization algorithms like method of moving asymptotes (MMA) [2] and structural optimization techniques as discussed in [3]. The optimality of the structure and continua from a material or from a microscopic material distribution or micro-structural point of view also started at the same time and many approaches have been proposed based on the homogenization techniques [4–6].

Continuous advancement in the field of topology optimization and development of new robust algorithms [7, 8] have lead to its expansion in other applications such as heat transfer [9, 10], piezoelectricity [11, 12] and most importantly multi-material optimization [13–15] in which the material distribution at the microscale is controlled along with the material distribution at macroscale for the minimization or maximization of some macroscopic objective. Optimization for the interface problems such as coated structures and material interfaces are done recently using the same topology optimization techniques [16]. In fluid mechanics similar studies have been conducted for Navier-Stokes [17] and Stokes [18] flows and optimal fluid flow path through the channel has been developed. One can also find intriguing studies on multi-physics problems dealing with fluid flow and heat transfer simultaneously such as in [19].

First attempt of optimization in hydrodynamic lubrication goes back to Lord Rayleigh in 1918 when he tried to come up with an optimum shape of the bearing for the maximum pressure generated [20]. Similar to it in [21] a minimum constraint was set on the fluid film height for the optimization of the shape of slider bearing and a maximum principle approach is applied for the optimization of one-dimensional journal bearing [22]. As an industrially very important problem, hard disk slider also got benefited from these optimization techniques and one can find multi-physics and multi-objective optimization problems for slider air bearing for hard disks in [23–31].

Reynolds equation satisfactorily reflects the lubrication physics and its solution delivers the pressure which carries the load on the interface [32, 33]. Recently, texture optimization using Reynolds equation has also been done in which partial or complete texturing of the interface is realized with pillar-type textures with different geometrical shapes [34–39]. However, unlike the case for multiscale optimization for materials like composites, optimization for macroscopic responses such as negative Poisson's ratio or a negative thermal expansion using homogenization techniques, the optimization for lubrication using homogenization techniques has not been investigated yet. Fairly complex micro-textures can now be fabricated with the advent of novel micro-fabrication techniques and one may use these in the lubrication interfaces instead of simple pillar or hole type textures. So, the goal of this research work is to develop a suitable computational scheme based on homogenization, for hydrodynamic lubrication using Reynolds equation, to come up with intriguing manufacturable micro-textures for lubrication interfaces.

The work is organized as follows; in **Chapter 2** the lubrication along with its regimes are defined as a sub-branch of tribology. Stokes equations are stated as a simplified form of the Navier-Stokes equations under the assumptions of the simplified fluid flow. Then the Reynolds equation is derived from the Stokes equation considering the assumption of very small fluid film height in lubrication devices. All the assumptions made for the derivation are stated explicitly.

Chapter 3 includes the Finite Element Formulation of the Reynolds equation to solve for the pressure response numerically in two-dimensions (as the two-dimensional Reynolds equation is valid for three-dimensional lubrication problem). Basic tensor calculus is introduced and based on it the weak form is derived for the discretization of the equation and finally a system of linear equations is evaluated by integrating the discretized equation for the solution of the problem.

Chapter 4 provides a framework for the computational homogenization of the Reynolds equation to separate the microscale from the macroscale and give an insight into how the microscale has an effect on the macroscale. Homogenization provides an inexpensive way to solve for the multiscale problems as compared to direct numerical solutions. Homogenization is done via well-established method of asymptotic expansion to separate the scales. Cell problems are defined on a unit-cell of roughness and a macroscopic equation is constructed for the solution of the macroscopic pressure which makes use of the homogenized coefficients calculated from the solution of the cell problems. Finally, different two-scale settings cases of unilateral roughness for hydrodynamic lubrication are discussed.

Chapter 5 is concerned with constructing a basis for optimization in hydrodynamic lubrication. Surface texture is defined via fluid film thickness such that by controlling the fluid film thickness a desired macroscopic response can be obtained via homogenized coefficients. Filter types are also discussed for the texture design and finally different types of microscopic and macroscopic optimization schemes are discussed in the end.

Chapter 6 investigates microscopic objective optimization. First, the optimization problem is defined and then the sensitivity of the homogenized coefficients are derived that appear in the sensitivity of the objective which has to be used in a gradient-based optimization algorithm. Default numerical settings are defined and optimum optimization parameters are found through the numerical simulations. After that the microscopic optimization for the texture reconstruction is done for the default textures. Finally, Onsager's principle is discussed with the examples and subsequently the sensitivity analysis is validated for selected optimized results.

Chapter 7 extends the microscopic objective optimization to the macroscale setting. Two macroscopic problems are defined, namely: squeeze film flow and the wedge problem. The micro-textures are reconstructed first as a sanity check of the optimization algorithm, the micro-textures are optimized for prescribed load bearing capacity of the interface and maximization of load bearing capacity for the squeeze film flow in temporal variations of the film thickness. Micro-texture optimization for the standard wedge problem is similarly realized in spatial variations of the film thickness and finally Taylor's expansion is used for the squeeze film flow considering the computational cost associated with the homogenization technique.

Chapter 8 provides the limitations and outlook of the current work.

Chapter 2

Lubrication Theory

In this chapter, first lubrication regimes are defined and the Stokes's equations are obtained from the Navier-Stokes N-S equations with underlying assumption of simplified fluid flow. Finally, the Reynolds equation is derived from Stokes equation based on the lubrication theory.

2.1 Tribology

Tribology is the science of the interaction of surfaces; it involves mainly the study of friction, wear and lubrication. Friction is the resistance to the relative motion of the interacting surfaces, it converts kinetic energy of the interacting surfaces in motion to thermal dissipation, vibration and sound energy. In some machine elements, friction governs the working mechanism. For example the connecting belt of the car engine is manufactured with grooves to maximize the friction between the belt and the shaft. On the other hand, energy loss due to friction is a major economical concern due to its presence where it is not desired. For instance, approximately one third of the fuel energy is wasted in overcoming the friction in passenger cars. Friction is strongly affected by unavoidable asperities present on the surfaces due to manufacturing process. These asperities are also the cause of slow erosion of the machine elements due to their interaction which eventually leads to mechanical failure. This erosion phenomena is called wear and it is almost never desired in a mechanical system. To reduce or eliminate friction and wear generally a fluid is introduced between the surfaces. This is called lubrication and it will be discussed in detail in the following sections.

2.2 Lubrication

Lubrication is a process in which the a lubricant, usually a fluid, is introduced between the two interacting surfaces moving relative to each other. Lubricatoin is applied to reduce the wear caused by the friction. The load is carried by the pressure generated within the fluid film and the frictional resistance to motion arises entirely from the shearing of the viscous fluid. Lubrication can be divided into four lubrication regimes, namely: Hydrodynamic lubrication, elastohydrodynamic lubrication, mixed (partial) lubrication and boundary lubrication.

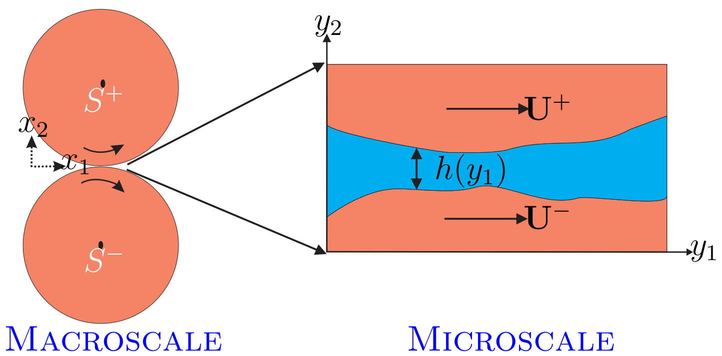

Figure 2.1: *The contact homogenization problem is summarized.*

Hydrodynamic Lubrication (HL): In hydrodynamic lubrication, the surfaces are conformal and the load is supported by the pressure generated in the fluid which does not exceed 5 MPa [40] and surface deformation is negligible because of the large load bearing area associated with the conformal surfaces. The surfaces do not come into contact because of the fluid film present whose thickness ranges from $1\mu m$ to $2.5\mu m$ in thin film and thick film lubrication, respectively.

Elastohydrodynamic Lubrication (EHL): It is a type of hydrodynamic lubrication in which surfaces are non-conformal and surface deformation is present due to high pressure. There are two types of EHL namely hard EHL and soft EHL. In hard EHL the interacting surfaces are with high elasticity modulus such as metals and in soft EHL the interacting surfaces are soft such as rubbers the pressure ranges from 0.5 to 3 GPa in hard elastohydrodynamic lubrication and 1 MPa in soft elastohydrodynamic lubrication. The minimum fluid film thickness normally exceeds 0.1 and 1.0 μm for hard and soft EHL, respectively.

Mixed Lubrication: It occurs when the pressure between the lubricated surfaces is too high or the relative motion is very slow, this causes the fluid film to vanish from the interface locally, and the asperities come into contact at some of the points. This type of lubrication is also known as partial lubrication. The fluid film thickness is of the order of 0.01 μm.

Boundary Lubrication (BL): This is a lubrication regime in which there is negligible fluid presence between the surfaces and the asperities are in contact considerably. Most of the load is carried by the surface boundaries hence the hydrodynamic lift is negligible. The fluid film thickness is about 1 - 10 nm.

In this study, only the hydrodynamic lubrication is considered and it is derived through the Navier-Stokes equations under the assumption of very thin fluid film.

2.3 Reynolds Equation

Reynolds equation governs the physics of lubrication and it is derived from the Navier-Stokes equations and continuity equation in the limit of vanishing fluid film thickness. The derivation is briefly outlined below.

2.3.1 Navier-Stokes Equations

It is assumed that the fluid in hydrodynamic lubrication behaves as Newtonian fluid and the shear rate of fluid can be represented linearly to the shear stress. Moreover, laminar flow is considered. After taking the surface forces, body forces, and inertia forces into account the N-S equations can be written as follows

$$\rho \boldsymbol{a} = \rho \left(\frac{\partial \boldsymbol{v}}{\partial t} + (\nabla \boldsymbol{v})\boldsymbol{v} \right) = -\nabla p + \rho \boldsymbol{g} + \mu \nabla^2 \boldsymbol{v} \tag{2.1}$$

The above equation is based on the assumptions that the temperature differences are small within the fluid, the viscosity μ of the fluid is constant and that the flow is incompressible. The terms on the left are the inertial terms and on the right side are the pressure gradient, body forces and viscous terms, respectively. Here, p is the fluid pressure, $\boldsymbol{v}$ is the fluid velocity, $\boldsymbol{a}$ is the acceleration, $\boldsymbol{g}$ is the body force and

$$\nabla^2 \boldsymbol{v} = \frac{\partial^2 v_1}{\partial x_1^2} + \frac{\partial^2 v_2}{\partial x_2^2} + \frac{\partial^2 v_3}{\partial x_3^2} \tag{2.2}$$

Here x_1, x_2 and x_3 are the directions in the cartesian coordinate system. In the above equation the velocity $\boldsymbol{v}$ and pressure p are the unknown fields. There are three equations present for three-dimensional (3D) fluid flow and four unknowns to solve for. The fourth equation will be provided by the mass conservation in fluid flow, which is provided by continuity equation.

2.3.2 Continuity Equation

It states that the fluid coming in a control volume of a fluid is equal to the fluid coming out of the control volume. Following is the differential form of the continuity equation.

$$\frac{\partial \rho}{\partial t} + \nabla \cdot (\rho \boldsymbol{v}) = 0 \tag{2.3}$$

For an *incompressible fluid* $\rho = \text{constant} > 0$. It is also assumed that the density of the fluid does not change spatially. Thus equation (2.3) takes the form [33]

$$\nabla \cdot \boldsymbol{v} = 0 \tag{2.4}$$

For basic concepts in tensor calculus the reader is referred to the Appendix A.

2.3.3 Stokes Equations

The Stokes equations are derived from the N-S equations (2.1), the small length scale of the problem leads towards negligible values of Reynolds number which is the ratio of inertial forces to viscous forces of fluid flow, $Re = \frac{\rho \bar{v} L}{\mu}$. Here ρ is the density of fluid, $\bar{v}$ is the mean velocity of the solid object relative to the fluid, μ is the dynamic viscosity of the fluid and L is the characteristic length. For thin film flow, the characteristic length is so small that the Reynolds number becomes very small. Therefore, the inertial forces are dominated by viscous forces. So, the left hand side of Equation (2.1) can be neglected. The body force term on the right hand side can also be neglected because of the small fluid film. The Stokes equations, to be complemented by the continuity equation, can be written as follows:

$$\mathbf{0} = -\nabla p + \mu \nabla^2 \boldsymbol{v} \tag{2.5}$$

2.3.4 Lubrication Theory

The film thickness along the vertical direction x_3 is extremely small with respect to the lateral dimensions in the x_1 - x_2 plane of the interface which makes the pressure change and velocity in x_3 direction negligible i.e., $\frac{\partial p}{\partial x_3} = 0$ and $v_3 = 0$. Under these assumptions, the Stokes equations reduce to the following simplied expressions:

$$
\begin{aligned}
x_1 &: \frac{\partial p}{\partial x_1} = \mu \frac{\partial^2 v_1}{\partial {x_3}^2} \\
x_2 &: \frac{\partial p}{\partial x_2} = \mu \frac{\partial^2 v_2}{\partial {x_3}^2}
\end{aligned}
\tag{2.6}
$$

The continuity equation is also reduces to two-dimensions

$$
\frac{\partial v_1}{\partial x_1} + \frac{\partial v_2}{\partial x_2} = 0 \tag{2.7}
$$

Assuming the surfaces are smooth and moving and solving Stokes equation results in

$$
\begin{aligned}
v_1 &= -x_3 \left(\frac{h - x_3}{2\mu} \right) \frac{\partial p}{\partial x_1} + {U_1}^{-} \left(\frac{h - x_3}{h} \right) + {U_1}^{+} \frac{x_3}{h} \\
v_2 &= -x_3 \left(\frac{h - x_3}{2\mu} \right) \frac{\partial p}{\partial x_2} + {U_2}^{-} \left(\frac{h - x_3}{h} \right) + {U_2}^{+} \frac{x_3}{h}
\end{aligned}
\tag{2.8}
$$

Here, U^+ is the velocity of upper surface, U^- is the velocity of the lower surface and h is the fluid film thickness as shown in Figure 2.1. To get rid of x_3 term we will integrate in x_3 direction and Stokes equations will result in fluid flux as follows

$$
\begin{aligned}
q_1 &= -\frac{h^3}{12\mu} \frac{\partial p}{\partial x_1} + \frac{{U_1}^{-} + {U_1}^{+}}{2} h, \\
q_2 &= -\frac{h^3}{12\mu} \frac{\partial p}{\partial x_2} + \frac{{U_2}^{-} + {U_2}^{+}}{2} h
\end{aligned}
\tag{2.9}
$$

Here, q_1 is the fluid flux in x_1 direction and similarly q_2 is the fluid flux in x_2 direction. Now, from the continuity equation (2.3) following form is obtained

$$
-\nabla \cdot \boldsymbol{q} = \frac{\partial h}{\partial t} \tag{2.10}
$$

Equation (2.10) and fluid flux in equation (2.9) with the definition $\boldsymbol{U} = \boldsymbol{U}^{-} + \boldsymbol{U}^{+}$ will result in the Reynolds Equation as follows

$$
\boxed{-\nabla \cdot \left(-\frac{h^3}{12\mu} \nabla p + \frac{\boldsymbol{U} h}{2} \right) = \frac{\partial h}{\partial t}} \tag{2.11}
$$

Reynolds equation assumes that the interacting surfaces are smooth. However, this is not the case, in reality the surface roughness is present and it can be catagories in two types: Stokes roughness and Reynolds roughness. In Stokes roughness the surface roughness is smaller than the film thickness (Stokes equation should be used in this case) [41] and in Reynolds roughness the surface roughness is larger than the film thickness (Reynolds equation is valid in this case) [42].

Chapter 3

Finite Element Formulation

In this chapter the Finite Element Method (FEM) formulation of Reynolds equation is presented. The weak form and FEM discretization of Reynolds equation is derived.

3.1 Weak Form of Reynolds Equation

The reader is referred to the Appendix A for basic tensor calculus. The strong form of the Reynolds equation for a domain Ω is given by (2.11). It is subject to the boundary conditions $p = \bar{p}$ at Γ^p and $q = \bar{q}$ at Γ^q. The strong form of this equation is hard to solve analytically in two-dimensions, so an approximate representation through a weak form will be discretized and solved. For obtaining the weak form the above equation can be written as

$$r = \nabla \cdot \boldsymbol{q} + \frac{\partial h}{\partial t} = \nabla \cdot \left(-\frac{h^3}{12\mu} \nabla p + \frac{\boldsymbol{U} h}{2} \right) + \frac{\partial h}{\partial t} = 0 \tag{3.1}$$

Introducing a test function η the weighted residual integral is stated as

$$R = \int_{\Omega} \eta (\nabla \cdot \boldsymbol{q} + \frac{\partial h}{\partial t}) d\Omega = 0 \tag{3.2}$$

The weighted residual form (3.2) is satisfied for all η. Using integration by parts, the weighted residual form for the first term in (3.2) is restated as follows

$$\int_{\Omega} \eta(\nabla \cdot \boldsymbol{q}) d\Omega = \int_{\Omega} \nabla \cdot (\eta \boldsymbol{q}) d\Omega - \int_{\Omega} \boldsymbol{q} \cdot (\nabla \eta) d\Omega \tag{3.3}$$

After applying the divergence theorem to the first term on the right hand side, one obtains

$$\int_{\Omega} \eta(\nabla \cdot \boldsymbol{q}) d\Omega = \int_{\Gamma} \eta(\boldsymbol{q} \cdot \boldsymbol{n}) dA - \int_{\Omega} (\nabla \eta) \cdot \boldsymbol{q} d\Omega \tag{3.4}$$

Defining $-\boldsymbol{q} \cdot \boldsymbol{n} = q_n$ on Γ^q as a Neumann boundary condition and invoking $\eta = 0$ on Γ^p, the weak form is obtained by substituting (3.4) into (3.3):

$$\boxed{\int_{\Omega} (\nabla \eta) \cdot \left(-\frac{h^3}{12\mu} \nabla p \right) d\Omega = \int_{\Omega} (\nabla \eta) \cdot \left(-\frac{\boldsymbol{U} h}{2} \right) d\Omega + \int_{\Omega} \eta \left(\frac{\partial h}{\partial t} \right) d\Omega - \int_{\Gamma^q} \eta q_n d\Gamma} \tag{3.5}$$

In the remainder of this work it is assumed that either $\Gamma^p = \Gamma$, i.e. the whole boundary, or $q_n = 0$.

3.2 FEM Discretization

The weighted residual form of the Reynolds equation is discretized by dividing the domain into a finite number of elements to obtain an approximated numerical result. Quadrilateral elements are used to discretize. If N_{ei} are the number of elements in x_i direction and N_{ni} are the number of nodes in that direction. Total number of elements N_e and nodes N_n in the discretized domain are as follows

$$\begin{aligned} N_e &= N_{e1} \times N_{e2} \\ N_n &= (N_{e1} + 1) \times (N_{e2} + 1) \end{aligned} \tag{3.6}$$

The element e_i is the $i - th$ element and e_i^I is the $I - th$ node of $i - th$ element.

3.2.1 Isoparametric Mapping

A master element domain $\mathcal{Z}$ is introduced to map the position x_i, pressure p and test function η using shape functions $\phi(\zeta_1, \zeta_2)$, where ζ_i is the coordinate of $\mathcal{Z}$ domain. The position in $\mathcal{Z}$ is projected into Ω domain.

$$x'_i = \sum_{I=1}^{4} x_i^{e^I} \phi_{e^I} \tag{3.7}$$

Here, $x_i^{e^I}$ corresponds to the coordinate of $I - th$ node of $e - th$ element in the domain Ω and x'_i is the corresponding integration point in the $\mathcal{Z}$ domain.

3.2.2 Gradients

The gradients of pressure (∇p) and the test function ($\nabla \eta$) are required to solve the weak form (3.3) of the Reynolds equation, these gradients can be written as a function of ζ_i because p is only known with respect to ζ_i. The gradient of the pressure is

$$\nabla p = \frac{\partial p}{\partial x_i} = \frac{\partial p}{\partial \zeta_j} \frac{\partial \zeta_j}{\partial x_i} \tag{3.8}$$

Then $\frac{\partial p}{\partial \zeta_j}$ become

$$\frac{\partial p}{\partial \zeta_j} = \sum_{I=1}^{4} p_I \frac{\partial \phi_I}{\partial \zeta_j} \tag{3.9}$$

Now, $\frac{\partial x_i}{\partial \zeta_j}$ can be evaluated using equation (3.7)

$$F_{ij} = \frac{\partial x_i}{\partial \zeta_j} = \sum_{I=1}^{4} x_i^I \frac{\partial \phi_I}{\partial \zeta_j} \tag{3.10}$$

This 2×2 matrix $\boldsymbol{F}$ is called gradient of mapping and its inverse is computable i.e., $\bar{\boldsymbol{F}} = \boldsymbol{F}^{-1}$. The terms on the left hand side of weak form (3.3) can be expanded as

$$(\nabla\eta)\cdot\left(\frac{h^3}{12\mu}\nabla p\right)=\frac{\partial\eta}{\partial x_k}\frac{h^3}{12\mu}\frac{\partial p}{\partial x_k}$$
$$=\frac{\partial\eta}{\partial\zeta_i}\bar{F}_{ik}\frac{h^3}{12\mu}\frac{\partial p}{\partial\zeta_j}\bar{F}_{jk} \tag{3.11}$$

A matrix $\bar{\boldsymbol{b}}$ is introduced such that $\bar{b}_{ij}=\bar{F}_{ik}\bar{F}_{jk}$. Substituting $\bar{b}_{ij}$ into (3.11) and making use of (3.10), the following is obtained

$$(\nabla\eta)\cdot\left(\frac{h^3}{12\mu}\nabla p\right)=\sum_I\sum_J\eta_I\frac{h^3}{12\mu}\frac{\partial\phi_I}{\partial\zeta_i}\bar{b}_{ij}\frac{\partial\phi_J}{\partial\zeta_j}p_j \tag{3.12}$$

Then, a 2×2 matrix $\boldsymbol{G}$ is defined as follows

$$G_{IJ}=\frac{\partial\phi_I}{\partial\zeta_i}\bar{b}_{ij}\frac{\partial\phi_J}{\partial\zeta_j} \tag{3.13}$$

Finally, the left hand side of the weak form is written

$$\int_\Omega(\nabla\eta)\cdot\left(\frac{h^3}{12\mu}\nabla p\right)d\Omega=\int_\Omega\sum_I\eta_I\left(\sum_J\frac{h^3}{12\mu}G_{IJ}p_J\right)d\Omega \tag{3.14}$$

Similarly, the right hand side of the weak form is written as

$$\int_\Omega(\nabla\eta)\cdot\left(\frac{-\boldsymbol{U}h}{2}\right)d\Omega=\int_\Omega\sum_I\eta_I\left(-\frac{\partial\phi_I}{\partial\zeta_i}\frac{\partial\zeta_i}{\partial x_i}U_j\frac{h}{2}\right)d\Omega \tag{3.15}$$

and

$$\int_\Omega\eta\frac{\partial h}{\partial t}d\Omega=\int_\Omega\sum_I\eta_I\phi_I\frac{\partial h}{\partial t}d\Omega \tag{3.16}$$

3.3 Numerical Integration

The integrals (3.14) and (3.15) are calculated numerically, Gaussian quadrature integration rule is used for this purpose. The volume mapping of the domain Ω to $\mathcal{Z}$ is done because the pressure p and the test functions η are discretized in this domain. Jacobian of mapping J is introduced for this purpose

$$J = det[\boldsymbol{F}] \tag{3.17}$$

And it can be shown that

$$d\Omega = Jd\mathcal{Z} \tag{3.18}$$

Numerical integration over the domain $\mathcal{Z}$ is evaluated as follows

$$\int_{\mathcal{Z}} f(\boldsymbol{\zeta})d\mathcal{Z} = \sum_{g_1=1}^{N_g}\sum_{g_2=1}^{N_g} w_{g_1}w_{g_2}f(\zeta_{g_1},\zeta_{g_2}) \tag{3.19}$$

Here, N_g is the number of Gauss points, w_{g_1} and w_{g_2} are the integration weights, and $(\zeta_{g_1},\zeta_{g_2})$ are the integration points at which the function f is evaluated. Applying (3.19) to (3.14) and (3.15) following are obtained

$$K_e(I,J) = \sum_{g_1=1}^{N_g}\sum_{g_2=1}^{N_g} w_{g_1}w_{g_2}\frac{h^3}{12\mu}J\sum_{I=1}^{4}\sum_{J=1}^{4}G(I,J) \tag{3.20}$$

$$B_e(I,1) = \sum_{g_1=1}^{N_g}\sum_{g_2=1}^{N_g} w_{g_1}w_{g_2}J\sum_{I=1}^{4}\left(-\frac{\partial\phi_I}{\partial\zeta_i}\frac{h}{2}\frac{\partial\zeta_i}{\partial x_j}U_j + \phi_I\frac{\partial h}{\partial t}\right) \tag{3.21}$$

Here, $K_e(I,J)$ is so-called element stiffness matrix and $B_e(I,1)$ is the element force vector. An assembly operator $\mathbb{A}$ is used to evaluate global stiffness matrix and force vector.

$$K = \mathbb{A}K_e \qquad and \qquad B = \mathbb{A}B_e \tag{3.22}$$

3.4 Linear System of Equations

After putting all of this information into equation (3.5) the test degree of freedom cancel each other out across the equality and the only unknown variable that remains is the pressure p, and finally following system of linear equation are obtained.

$$Kp = B \tag{3.23}$$

One may use direct or iterative solvers to obtain the solution $p = K^{-1}B$ after applying Dirichlet boundary conditions.

Chapter 4

Homogenization of the Reynolds Equation

This chapter deals with the homogenization of Reynolds equation in unilateral settings. The asymptotic expansion method is used for homogenization which involves the use of scale separation. Cell problems and homogenized coefficients are defined for the homogenized equation. Finally, the unilateral settings are explained and an explicit formulation of homogenization equation is presented for its use in optimization.

4.1 Two-scale settings

In the present study hydrodynamic lubrication is considered in which there is no partial contact, cavitation or turbulence present. Furthermore, the Reynolds roughness is assumed true so that the homogenization based on scale separation can be employed. Equation (2.11) is very easy to solve for the pressure response when the film thickness is not oscillating, but this is not the case in reality because the film thickness oscillates due to surface roughness present at multiple scales. This oscillations in the surface roughness makes the film thickness also to oscillate locally and hence the resulting pressure is also highly oscillatory. These oscillations can not be omitted and should be solved by using a heterogeneous Reynolds equation (4.1) which is computationally very expensive.

$$-\nabla_{\boldsymbol{x}_\varepsilon} \cdot \boldsymbol{q}(\boldsymbol{x}_\varepsilon, t_\varepsilon) = 0 \tag{4.1}$$

Presently the $\frac{\partial h_\varepsilon(\boldsymbol{x}_\varepsilon, t_\varepsilon)}{\partial t_\varepsilon}$ term is omitted from the above equation, which omits the local oscillation of the solution due to time and the detailed reasons are presented in section (4.4), this makes Reynolds equation time-independent. In equation (4.1) $\boldsymbol{x}_\varepsilon$ and t_ε are the absolute position and time. The interface fluid flux $\boldsymbol{q}(\boldsymbol{x}_\varepsilon, t_\varepsilon)$ depends on the fluid film thickness $h_\varepsilon(\boldsymbol{x}_\varepsilon, t_\varepsilon)$ via

$$\boldsymbol{q}(\boldsymbol{x}_\varepsilon, t_\varepsilon) = -\frac{h^3}{12\mu}\boldsymbol{g}_\varepsilon + \frac{h_\varepsilon}{2}\boldsymbol{U} \tag{4.2}$$

where μ is the fluid viscosity and $\boldsymbol{g}_\varepsilon = \nabla_{\boldsymbol{x}_\varepsilon} p_\varepsilon$. $\varepsilon \ll 1$ is a scale factor that is proportional to the roughness wavelength and indicates highly oscillatory quantities. Equation (4.1) is computationally expensive to solve because of the high finite element resolution required for finding the deterministic solution. So, an alternative solution through asymptotic homogenization, will be sought for less expansive and fast computation which is also perfectly suitable for texture optimization. In asymptotic homogenization ε is employed to invoke the two-scale separation as it approaches to a very small value. The two-scale expressions for space is written as follows

$$\boldsymbol{x}_\varepsilon = \boldsymbol{x} + \varepsilon \boldsymbol{y} \tag{4.3}$$

where $\boldsymbol{x}$ is the coarse scale (macroscopic) position while $\boldsymbol{y}$ is its independent fine scale (microscopic) counterpart. The film thickness is then assigned the form

$$h_\varepsilon(\boldsymbol{x}_\varepsilon) = h(\boldsymbol{x}, \boldsymbol{y}) = h_0(\boldsymbol{x}) + h^+(\boldsymbol{y}) - h^-(\boldsymbol{y}) \tag{4.4}$$

where h_0 describes the smooth macroscopic variation of the film thickness while $h^\mp$ are the roughness contributions with zero mean from the upper and lower surfaces. Now, the pressure is asymptotically expanded as

$$p_\varepsilon(\boldsymbol{x}_\varepsilon) = p_0(\boldsymbol{x}, \boldsymbol{y}) + \varepsilon p_1(\boldsymbol{x}, \boldsymbol{y}) + \varepsilon^2 p_2(\boldsymbol{x}, \boldsymbol{y}) + \mathcal{O}(\varepsilon^3). \tag{4.5}$$

where $p_0(\boldsymbol{x},\boldsymbol{y})$ is the macroscale contribution and and $p_i(\boldsymbol{x},\boldsymbol{y})$, $i = 1, 2, ..$ are microscale corrector contributions. It is noted that $\nabla_{\boldsymbol{x}_\varepsilon}$ may be expressed

$$\nabla_{\boldsymbol{x}_\varepsilon} = \frac{d}{d\boldsymbol{x}_\varepsilon} = \frac{\partial}{\partial \boldsymbol{x}} + \frac{1}{\varepsilon}\frac{\partial}{\partial \boldsymbol{y}} = \nabla_{\boldsymbol{x}} + \varepsilon^{-1}\nabla_{\boldsymbol{y}} \tag{4.6}$$

4.2 Cell Problems

The scale separation is invoked via $\varepsilon \to 0$ after putting (4.2) – (4.6) into (4.1) leading to

$$(\nabla_{\boldsymbol{x}} + \varepsilon^{-1}\nabla_{\boldsymbol{y}}) \cdot \left[\frac{h^3}{12\mu}(\nabla_{\boldsymbol{x}} + \varepsilon^{-1}\nabla_{\boldsymbol{y}})(p_0 + \varepsilon p_1 + \varepsilon^2 p_2 + ...) - \frac{\boldsymbol{U}}{2} \cdot (\nabla_{\boldsymbol{x}} + \varepsilon^{-1}\nabla_{\boldsymbol{y}})h\right] = 0 \tag{4.7}$$

Expanding (4.7) and defining the following operators

$$\begin{aligned}
A_0 &= \nabla_{\boldsymbol{x}} \cdot \left(\frac{h^3}{12\mu}\nabla_{\boldsymbol{x}}\right) \\
A_1 &= \nabla_{\boldsymbol{y}} \cdot \left(\frac{h^3}{12\mu}\nabla_{\boldsymbol{x}}\right) + \nabla_{\boldsymbol{x}} \cdot \left(\frac{h^3}{12\mu}\nabla_{\boldsymbol{y}}\right) \\
A_2 &= \nabla_{\boldsymbol{y}} \cdot \left(\frac{h^3}{12\mu}\nabla_{\boldsymbol{y}}\right)
\end{aligned} \tag{4.8}$$

the following is obtained

$$\begin{aligned}
\varepsilon^0(A_0p_0 + A_1p_1 + A_2p_2) + \varepsilon^{-1}(A_1p_0 + A_2p_1) + \varepsilon^{-2}A_2p_0 + \mathcal{O}(\varepsilon) = \\
\varepsilon^0\left[\frac{\boldsymbol{U}}{2} \cdot (\nabla_{\boldsymbol{x}}h)\right] + \varepsilon^{-1}\left[\frac{\boldsymbol{U}}{2} \cdot (\nabla_{\boldsymbol{y}}h)\right]
\end{aligned} \tag{4.9}$$

Equating the terms with the same power of ε delivers three equalitites:

$$\varepsilon^{-2} \to A_2p_0 = 0 \tag{4.10}$$

$$\varepsilon^{-1} \to A_1p_0 + A_2p_1 = \frac{\boldsymbol{U}}{2} \cdot (\nabla_{\boldsymbol{y}}h) \tag{4.11}$$

$$\varepsilon^0 \to A_0p_0 + A_1p_1 + A_2p_2 = \frac{\boldsymbol{U}}{2} \cdot (\nabla_{\boldsymbol{x}}h) \tag{4.12}$$

These equations will be used to obtain the cell problems and homogenized Reynolds equation.

Equation 4.10: It implies that the first term in the expansion of pressure p_0 is independent from microscale variations,

$$p_0(\boldsymbol{x}, \boldsymbol{y}) = p_0(\boldsymbol{x}) \tag{4.13}$$

Equation 4.11: Reynolds equation at the microscale will be obtained which will have four microscopic solutions, so-called microscopic corrector terms. Substituting the values of A_1 and A_2 into (4.11) and making use of the result of (4.10), the following problem will be obtained

$$\nabla_{\boldsymbol{y}} \cdot \left(\frac{h^3}{12\mu} \nabla_{\boldsymbol{x}} p_0 \right) + \nabla_{\boldsymbol{y}} \cdot \left(\frac{h^3}{12\mu} \nabla_{\boldsymbol{y}} p_1 \right) = \frac{\boldsymbol{U}}{2} \cdot (\nabla_{\boldsymbol{y}} h). \tag{4.14}$$

Now upon linearly expanding the p_1 in terms of macroscopic pressure gradient $\boldsymbol{G}(\boldsymbol{x}) = \nabla_{\boldsymbol{x}} p_0$ and the relative velocity $\boldsymbol{V} = \boldsymbol{U}^+ - \boldsymbol{U}^-$ via

$$p_1 = \boldsymbol{G} \cdot \boldsymbol{\omega} - \boldsymbol{V} \cdot \boldsymbol{\Omega} \tag{4.15}$$

By substituting the expression of p_1 and noting that $\nabla_{\boldsymbol{x}} p_0(\boldsymbol{x}) = \frac{\partial p_0}{\partial x_1} \boldsymbol{e}_1 + \frac{\partial p_0}{\partial x_2} \boldsymbol{e}_2$, one obtains

$$\nabla_{\boldsymbol{y}} \cdot \left(\frac{h^3}{12\mu} \nabla_{\boldsymbol{y}} \left(\boldsymbol{G} \cdot \boldsymbol{\omega} - \boldsymbol{V} \cdot \boldsymbol{\Omega} \right) \right) = \frac{\boldsymbol{U}}{2} \cdot (\nabla_{\boldsymbol{y}} h) - \nabla_{\boldsymbol{y}} \cdot \left(\frac{h^3}{12\mu} \left(\frac{\partial p_0}{\partial x_1} \boldsymbol{e}_1 + \frac{\partial p_0}{\partial x_2} \boldsymbol{e}_2 \right) \right) \tag{4.16}$$

Now, equating the terms according to the directions four **cell-problems** are obtained as follows

$$\nabla_{\boldsymbol{y}} \cdot \left(\frac{h^3}{12\mu} \nabla_{\boldsymbol{y}} (\omega_1 \frac{\partial p_0}{\partial x_1}) \right) = -\nabla_{\boldsymbol{y}} \cdot \left(\frac{h^3}{12\mu} \frac{\partial p_0}{\partial x_1} \right), \tag{4.17}$$

$$\nabla_{\boldsymbol{y}} \cdot \left(\frac{h^3}{12\mu} \nabla_{\boldsymbol{y}} (\omega_2 \frac{\partial p_0}{\partial x_2}) \right) = -\nabla_{\boldsymbol{y}} \cdot \left(\frac{h^3}{12\mu} \frac{\partial p_0}{\partial x_2} \right), \tag{4.18}$$

$$\nabla_{\boldsymbol{y}} \cdot \left(\frac{h^3}{12\mu} \nabla_{\boldsymbol{y}} (-\Omega_1 V_1) \right) = \nabla_{\boldsymbol{y}} \cdot \left(\frac{U_1 h}{2} \right), \tag{4.19}$$

$$\nabla_{\boldsymbol{y}} \cdot \left(\frac{h^3}{12\mu} \nabla_{\boldsymbol{y}} (-\Omega_2 V_2) \right) = \nabla_{\boldsymbol{y}} \cdot \left(\frac{U_2 h}{2} \right). \tag{4.20}$$

By following [43] and canceling the similar term across the equality these cell problems can be written as follows

$$\frac{\partial}{\partial y_i} \left(\frac{h^3}{12\mu} \lambda_i^j \right) = -\frac{\partial}{\partial y_j} \left(\frac{h^3}{12\mu} \right) \quad , \quad \frac{\partial}{\partial y_i} \left(\frac{h^3}{12\mu} \Lambda_i^j \right) = -\frac{\partial}{\partial y_j} \left(\frac{h^+ + h^-}{2} \right) \tag{4.21}$$

where, $\lambda_i^j = \frac{\partial \omega_j}{\partial y_i}$, $\Lambda_i^j = \frac{\partial \Omega_j}{\partial y_i}$ and $i, j = 1, 2$. Here, $\omega_1, \omega_2, \Omega_1$ and Ω_2 together constitute the solution of these cell problems.

4.3 Homogenized Equation

Equation 4.12: Plugging the operators A_0, A_1 and A_2 into (4.12), the following equation is obtained:

$$\begin{aligned} \nabla_{\boldsymbol{x}} \cdot \left(\frac{h^3}{12\mu} \nabla_{\boldsymbol{x}} p_0 \right) + \nabla_{\boldsymbol{y}} \cdot \left(\frac{h^3}{12\mu} \nabla_{\boldsymbol{x}} p_1 \right) + \nabla_{\boldsymbol{x}} \cdot \left(\frac{h^3}{12\mu} \nabla_{\boldsymbol{y}} p_1 \right) + \\ \nabla_{\boldsymbol{y}} \cdot \left(\frac{h^3}{12\mu} \nabla_{\boldsymbol{y}} p_2 \right) = \frac{\boldsymbol{U}}{2} \cdot (\nabla_{\boldsymbol{x}} h) \end{aligned} \tag{4.22}$$

Averaging (4.22) over the periodic microscale domain $\mathcal{Y}$, the homogenized Reynolds equation for stationary incompressible case is obtained. During averaging the second and fourth term from the left hand side of (4.22) will become zero. Now putting the value of p_1 and expanding the differential to indicate directions following is obtained:

$$\begin{aligned} \nabla_{\boldsymbol{x}} \cdot \left(\frac{1}{|Y|} \int_Y \frac{h^3}{12\mu} \left(\frac{\partial p_0}{\partial x_1} \boldsymbol{e}_1 + \frac{\partial p_0}{\partial x_2} \boldsymbol{e}_2 \right) dy \right) + \\ \nabla_{\boldsymbol{x}} \cdot \left(\frac{1}{|Y|} \int_Y \frac{h^3}{12\mu} \nabla_{\boldsymbol{y}} \left(\frac{\partial p_0}{\partial x_1} \omega_1 + \frac{\partial p_0}{\partial x_2} \omega_2 \right) dy \right) = \\ \nabla_{\boldsymbol{x}} \cdot \left(\frac{1}{|Y|} \int_Y \left(\frac{\boldsymbol{U}}{2} h + \frac{h^3}{12\mu} (\nabla_{\boldsymbol{y}} . \boldsymbol{\Omega}) \boldsymbol{V} \right) dy \right) \end{aligned} \tag{4.23}$$

Above equation can be written in matrix form as:

$$-\nabla_{\boldsymbol{x}} \cdot \boldsymbol{Q} = 0 \tag{4.24}$$

(4.24) is the homogenized Reynolds equation where p_0 is the desired solution. Here, macroscopic flux Q has the form

$$\boldsymbol{Q} = -\boldsymbol{A}\boldsymbol{G} + \frac{h_0}{2}\boldsymbol{U} + \boldsymbol{B}\boldsymbol{V} \tag{4.25}$$

The tensors $\boldsymbol{A}$ and $\boldsymbol{B}$ are defined through

$$A_{ij} = \left\langle \frac{h^3}{12\mu}\left(\delta_{ij} + \lambda_i^i\right)\right\rangle \quad , \quad B_{ij} = \left\langle \frac{h^3}{12\mu}\Lambda_i^j \right\rangle \tag{4.26}$$

Here, δ_{ij} is the Kronecker delta, which refers to the components of the identity tensor $\boldsymbol{I}$. The seond and third term in (4.25), without the velocities included, can be written together with a single tensor as

$$\boldsymbol{C} = \frac{h_0}{2}\boldsymbol{I} + \boldsymbol{B} \tag{4.27}$$

4.4 Unilateral Roughness Settings

Unsteady hydrodynamic lubrication regime is obtained when both surfaces are rough and move tangentially relative to each other. This makes the homogenized coefficients $\boldsymbol{A}$ and $\boldsymbol{B}$ oscillate at a fixed point in the interface. To cope with these oscillations which have to be resolved, which can have significant effect on the pressure field [43], an assumption that one surface is rough is put forward. This makes the oscillations vanish and two lubrication regimes arise from this setting *stationary* hydrodynamic lubrication in which rough surface is stationary and smooth surface is moving, and *quasi-stationary* hydrodynamic lubrication in which rough surface is moving as well. In this work these later two regimes are considered.

Now referring to (Fig. 4.1) the special case of a periodic cell is considered in which lower surface ($\mathcal{S}^-$) is rough with $h^- = \overline{h}(\boldsymbol{y})$ as well as stationary while the upper

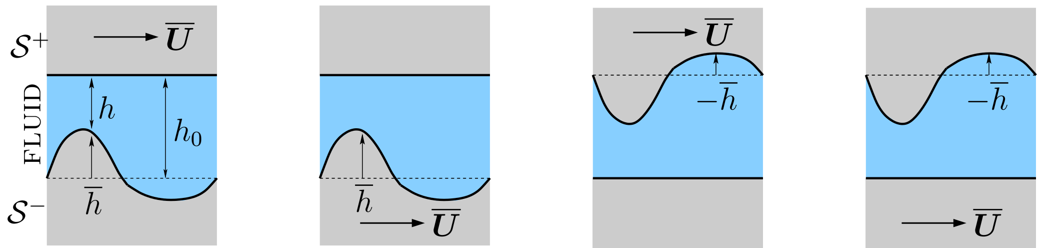

Figure 4.1: *Four different cases regarding the stationary and quasi-stationary regimes are depicted on a periodic cell.*

surface ($\mathcal{S}^+$) is smooth and moving with velocity $\boldsymbol{U}^+ = \overline{\boldsymbol{U}}$. The homogenized coefficient tensors $\boldsymbol{A} = \overline{\boldsymbol{A}}$ and $\boldsymbol{B} = \overline{\boldsymbol{B}}$ are obtained by solving the aforementioned cell problems. One more important conclusion here is by making use of only one rough surface the velcoity difference is becomes equal to the total velocity as well i.e., $\boldsymbol{V} = \overline{\boldsymbol{U}}$. By defining a vector $\boldsymbol{b} = \left(h_0/2\,\boldsymbol{I} + \overline{\boldsymbol{B}}\right)\overline{\boldsymbol{U}}$, or $\boldsymbol{b} = \boldsymbol{C}\overline{\boldsymbol{U}}$ the flux becomes

$$\boldsymbol{Q} = -\boldsymbol{A}\boldsymbol{G} + \boldsymbol{b} \tag{4.28}$$

In all of these cases either h^- or $-h^+$ equals $\overline{h}$ and either $\boldsymbol{U}^-$ or $\boldsymbol{U}^+$ equals $\overline{\boldsymbol{U}}$. It can be observed that all the four cases share the same $\boldsymbol{A} = \overline{\boldsymbol{A}}$ because $h = h_0 - \overline{h}$ distribution is the same in all of them but for the case of $\boldsymbol{b} = \boldsymbol{C}\overline{\boldsymbol{U}}$, the tensor $\boldsymbol{B}$ either has to be with a positive or a negative sign i.e., $\boldsymbol{C} = h_0/2\,\boldsymbol{I} \pm \overline{\boldsymbol{B}}$ this sign depends on which surface is rough and which one is moving. CASE 1 and CASE 2 result in the same $\boldsymbol{A}$ and $\boldsymbol{B}$ because they share the same $h = h_0 - \overline{h}$ and $h^+ + h^- = h^- = \overline{h}$ distribution the tensor $\boldsymbol{C}$ which will be obtained in the end will also be the same because of the fact that the minus sign in $\boldsymbol{C}$ will change to a positive because of $\boldsymbol{V} = -\overline{\boldsymbol{U}}$. Similar conclusion can be deduced for CASE 3 and CASE 4. Now, to compare CASE 1 and CASE 3 again the tensors $\boldsymbol{A}$ and $\boldsymbol{B}$ will be analyzed, the difference here from CASE 3 is that the $h^+ + h^- = h^+ = -\overline{h}$ which changes the sign of $\boldsymbol{B} = -\overline{\boldsymbol{B}}$ itself. Moreover, it will also change the sign within $\boldsymbol{C}$ as well i.e., $\boldsymbol{C} = h_0/2\,\boldsymbol{I} - \overline{\boldsymbol{B}}$, hence giving the same result at the end. So if $\boldsymbol{A}$ and $\boldsymbol{B}$ are known one can solve for all the four cases shown in (Fig. 4.1).

Bilateral motion of the surfaces can also be addressed. In CASE 1 let the lower surface have a velocity $\boldsymbol{U}^{-}$ the upper surface velocity is $\boldsymbol{U}^{+} = \boldsymbol{U}^{-} + \overline{\boldsymbol{U}}$ implies that $\boldsymbol{U} = 2\boldsymbol{U}^{-} + \overline{\boldsymbol{U}}$ and $\boldsymbol{V} = \overline{\boldsymbol{U}}$. Then one can obtain $\boldsymbol{b} = h_0 \boldsymbol{U}^{-} + (h_0/2\, \boldsymbol{I} + \boldsymbol{B})\overline{\boldsymbol{U}}$ using the two-scale expansion of height (4.4). Consequently, $\boldsymbol{b} - h_0\boldsymbol{U}^{-}$ is the Couette contribution which does not account for the rigid translation of fluid and is expressed in the form $\boldsymbol{C}\overline{\boldsymbol{U}}$.

For all the analysis and optimization in this work CASE 1 is considered in terms of $\boldsymbol{A}$ and $\boldsymbol{C}$ in view of its generality. Now, recalling $\langle h \rangle = h_0$ following can be written

$$C_{ij} = \left\langle \frac{h}{2}\delta_{ij} + \frac{h^3}{12\mu}\Lambda_i^j \right\rangle \tag{4.29}$$

where, Λ_i^j satisfies

$$\frac{\partial}{\partial y_i}\left(\frac{h^3}{12\mu}\Lambda_i^j\right) = -\frac{\partial}{\partial y_j}\left(\frac{h}{2}\right) \quad , \tag{4.30}$$

which leads to a specialized macroscopic flux expression

$$\boldsymbol{Q} = -\boldsymbol{A}\boldsymbol{G} + \boldsymbol{C}\boldsymbol{U} \quad . \tag{4.31}$$

Now, these homogenized coefficients $\boldsymbol{A}$ and $\boldsymbol{C}$ appearing in (4.31) can be tuned to get a desired pressure response. This fine tuning of the homogenized coefficients will be realized by indirectly controlling the surface texture through heights h.

Chapter 5

Optimization

The basis of optimization problem is presented in this chapter. First, a design variable is defined through which the surface texture can be controlled and hence the homogenized tensors. Then, an intermediate filtering process is explained for the design variables to obtain textures, in the sense that they have a well-defined length scale embedded in them despite their complex geometry. Finally, different types of optimization formulations are discussed for microscopic and macroscopic objectives.

5.1 Texture Design

The optimization process will make use of homogenized coefficients $\boldsymbol{A}$ and $\boldsymbol{C}$ which depend on the microscopic surface texture or roughness. Hence, by controlling the surface texture one can obtain the desired macroscopic response for (4.31). The surface texture can be defined by the fluid film thickness h that presently has the form (4.4). The surface textures should have specific characteristics from an engineering point of view. These characteristics can be the minimum-maximum texture height, the size and orientation of features. For this purpose the design variables $s^I \in [0, 1]$ are introduced to control the fluid film height distribution and hence the surface texture. In this work two discretization schemes will be discussed via shape functions N^I. These shape functions can either be of element wise-constant (S0) type [44] or of continuous piece-wise linear approximation (S1) type [45]. In either case, one may write

$$s = \sum_I N^I s^I \tag{5.1}$$

Linear Lagrange elements (Q1) are used for the discretization of the corrector terms $\boldsymbol{\omega}$ and $\boldsymbol{\Omega}$, the microscopic problems, and calculation of the homogenized coefficients. This leads toward two type of descritization possibilities (see Fig. 5.1) for microscopic texture optimization: (Q1S0) and (Q1S1) . The former provides less degree of freedom and prone to more numerical discrepancies than the latter one. For more detailed analysis on the choice of elements and their affect on the optimization process and end results reader is referred to the article [46].

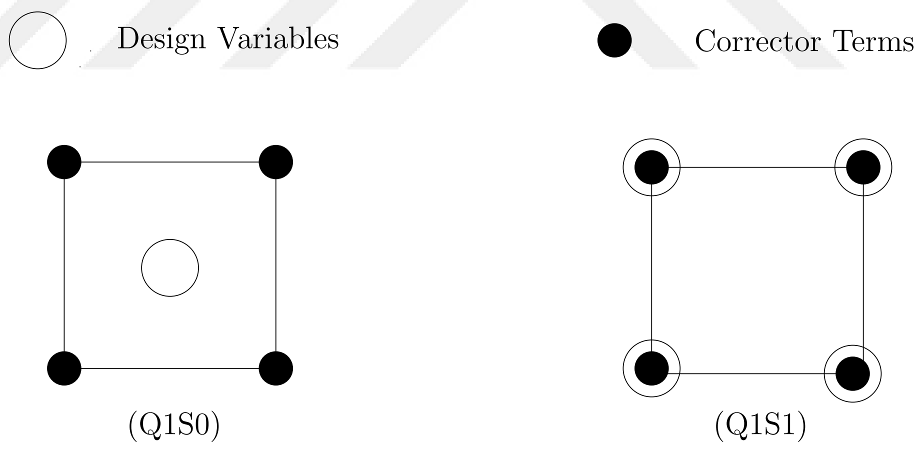

Figure 5.1: *Four different cases regarding the stationary and quasi-stationary regimes are depicted on a periodic cell.*

The design variable s will not be used as it is for defining the fluid film thickness. Rather, an intermediate filtering step will be employed. The filtering step $\mathcal{F}$ will deliver the filtered degree of freedom $\rho^K \in [0, 1]$. Filtered design variables are called morphology variables in their literature and the discretization is the same as that of s. The morphology filter $\mathcal{F}$ works on the the degree of freedom of s on a neighborhood $\mathcal{D}^K$ to deliver the new filtered degree of freedom ρ^K of the morphology variable ρ:

$$\rho = \sum_K N^K \rho^K = \sum_K N^K \mathcal{F}(\mathcal{D}^K, s) \quad . \tag{5.2}$$

This intermediate filtering is performed on the design variables s because without filtering the final design is prone to numerical discrepancies such as checker-board type oscillations [47]. To avoid these issues and also to embed a feature size into the texture, filtering is employed. In this work some of the filtering techniques introduced in [48] will be used. Sensitivity filter, which is widely used in topology optimization of structures, is found to give aesthetically less desirable designs and was also found to lead to a slow optimization process in the context of the present work. These selected filters along with their sensitivities are presented in (Table 5.1). A weighting factor $\omega^{KI} \in [0,1]$ is used to make sure that the ρ^K remains in the desired design limits [0, 1]. These weights can be of constant or conic type — for a detailed discussion, see [48]. The conic filter decreases its weight as it goes far form the filtering center I. The conic weights can be written as follows

$$w^{KI} = \begin{cases} \frac{R-d(K,I)}{\sum_{J\in\mathcal{D}^J} R-d(K,J)} & I \in \mathcal{D}^K \\ 0 & I \neq \mathcal{D}^K \end{cases} \tag{5.3}$$

Note that the $\sum_I w^{KI} = 1$. Here, $\mathcal{D}^K$ is the set of nodes I which are $d(K,I)$ distance away from the node K, this distance being equal to or less than the filtering radius R.

5.2 Texture Description

At the microscopic interface the fluid film thickness has minimum and maximum heights h_{min} and h_{max}, respectively. It is desired for the design texture to remain in between these fluid film heights. This is ensured by formulating the microscopic

Table 5.1: *Selected Linear, Harmonic, Geometric and Exponential type filters along with their sensitivities with respect to design variables.*

Method	*Filter* $\rho^K = \mathcal{F}(\mathcal{D}^K, s)$	*Sensitivity* $\frac{\partial \rho^K}{\partial s^I}$
Linear	$\rho^K = \sum_I w^{KI} s^I$	w^{KI}
Harmonic Erode	$\frac{1}{\rho^K+\alpha} = \sum_I \frac{w^{KI}}{s^I+\alpha}$	$w^{KI} \frac{\left(\rho^K+\alpha\right)^2}{(s^I+\alpha)^2}$
Harmonic Dilate	$\frac{1}{1-\rho^K+\alpha} = \sum_I \frac{w^{KI}}{1-s^I+\alpha}$	$w^{KI} \frac{\left(1-\rho^K+\alpha\right)^2}{(1-s^I+\alpha)^2}$
Geometric Erode	$\ln\left(\rho^K + \alpha\right) = \sum_I w^{KI} \ln\left(s^I + \alpha\right)$	$w^{KI} \frac{\left(\rho^K+\alpha\right)}{(s^I+\alpha)}$
Geometric Dilate	$\ln\left(1 - \rho^K + \alpha\right) = \sum_I w^{KI} \ln\left(1 - s^I + \alpha\right)$	$w^{KI} \frac{\left(1-\rho^K+\alpha\right)}{(1-s^I+\alpha)}$
Exponential Erode	$e^{\alpha(1-\rho^K)} = \sum_I w^{KI} e^{\alpha\left(1-s^I\right)}$	$w^{KI} \frac{e^{\alpha\left(1-s^I\right)}}{e^{\alpha(1-\rho^K)}}$
Exponential Dilate	$e^{\alpha\rho^K} = \sum_I w^{KI} e^{\alpha s^I}$	$w^{KI} \frac{e^{\alpha s^I}}{e^{\alpha\rho^K}}$

fluid film thickness in terms of morphology variables ρ as

$$h(\rho) = h_{\min} + (h_{\max} - h_{\min})\rho^{\eta} \quad \in [h_{\min}, h_{\max}] \tag{5.4}$$

Here, $\eta \geq 1$, so-called penalty parameter, is used to control the smoothness of the texture. A texture with smooth transitions between h_{min} and h_{max} is obtained if $\eta = 1$. This type of design is called 0-TO-1 design. On the other hand to obtain a texture with sharp transitions $\eta \geq 1$ is used, a common choice being $\eta = 3$ is utilized. This type of design will be reffered to as 0-OR-1 design. For a detailed analysis of the penalty parameter the reader is referred to [44]. These two designs schemes are depicted in Fig. 5.2. The upper row represents the 0-OR-1 design with yellow as maximum texture height (and minimum fluid film thickness h_{min}), and gray representing minimum texture height (and maximum fluid film thickness h_{max}). In the lower row 0-TO-1 design color scheme is shown with red representing the maximum texture heights (and minimum fluid film thickness h_{min}), and blue for minimum texture height (and maximum fluid film thickness h_{max}). These designs are presented in 2D tiled and 2D unit-cell 3D unit-cell and 3D tiled from left to right, with a Gray transparent surface on top of the 3D tiled to visualize how the interface look like for CASE-1 presented in (Sec. 4.4).

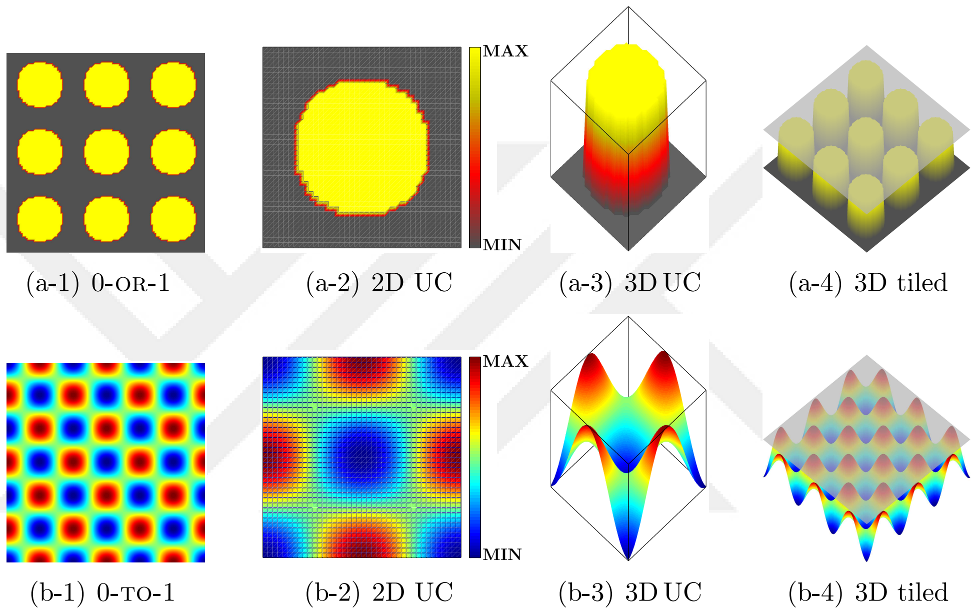

Figure 5.2: *Visualization and color schemes for* 0-OR-1 *(top row) and* 0-TO-1 *(bottom row) designs.*

5.3 Optimization Problem

Once the surface texture is defined through the fluid film thickness by controlling the design variable, one can achieve the desired macroscopic response in terms of homogenized tensors $\boldsymbol{A}$ and $\boldsymbol{C}$ or the macroscopic pressure response p_0. In this work two types of optimization problems are conducted in hydrodynamic lubrication. The first one, in which homogenized tensors are optimized, is called

Microscopic Objective Optimization (MicOO), because these homogenized coefficients are directly controlled by fluid film thickness h_0 and there is no macroscopic calculation of flux is involved. The second one is called Macroscopic Objective Optimization (MacOO). In this optimization problem the macroscopic fluid pressure is optimized by controlling the microscopic fluid film thickness so it involves the calculation of macroscopic pressure. Therefore, it is controlled indirectly through the homogenized coefficients over the whole lubrication interface via fluid film thicknesses variation. These two types of optimization problems (see Fig. 5.3) will be discussed in the following chapters in details with numerical examples. Six different types of optimization cases can be created by these two of optimization problems — see Table 5.2.

Table 5.2: *Description of different optimization scenarios for* MicOO *and* MacOO *shown in Fig. 5.3.*

Points in Fig. 5.3	*Description*
1 → 4	Texture reconstruction for microscopic objective.
1 → 2 → 3 → 4	Texture reconstruction for macroscopic objective.
2 → 3 → 4	Texture optimization for prescribed load bearing capacity.
3 → 4	Texture optimization for maximum load bearing capacity for temporal variations.
3 → 4	Texture optimization for maximum load bearing capacity for spatial variations.

First the reconstruction of the micro-textures are done for both MicOO and MacOO, the first two optimization cases in (Tab. 5.2), in which the homogenized macroscopic responses in terms of $\boldsymbol{A}^*$, $\boldsymbol{B}^*$ or p_0^* are calculated by inputting a target micro-texture and through optimization process micro-textures are reconstructed. These two optimization problems can be called the sanity checks of the optimization algorithm. The optimization then can be carried out for attaining a prescribed load bearing capacity, maximizing the load bearing capacity for both temporal and spatial variations of the film thickness across the macroscopic interface.

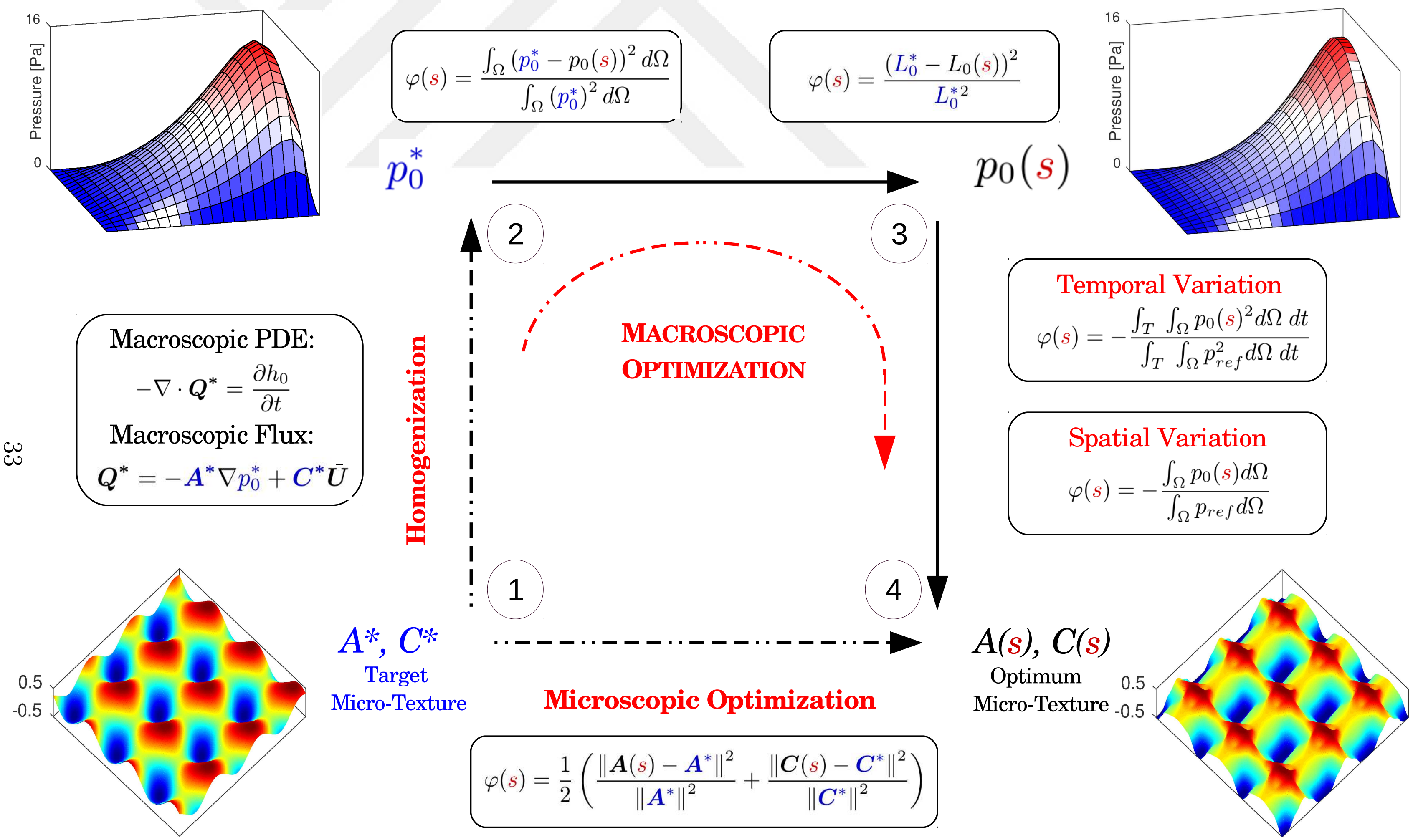

Figure 5.3: MicOO *and* MacOO *optimization problems with different optimization cases.*

Chapter 6

Microscopic Objective Optimization

In this chapter the reconstruction of micro-textures is carried out. First the optimization problem is formulated for MicOO and then the sensitivity analysis is carried out for the gradient-based optimization. Default numerical choices and optimization parameters such as filter type and filter radius etc., are selected. Finally, Onsager's principle is tested for micro-texture reconstruction.

6.1 Optimization Problem

To check the sanity and establishing the basis of optimization in hydrodynamic lubrication, the reconstruction of micro-textures using MicOO is carried out in which, the target homogenized coefficients $\boldsymbol{A}^*$ and $\boldsymbol{C}^*$ are obtained through a target micro-texture. These target homogenized coefficients then feed into optimization routine and the difference between the current and the target. The following objective is formulated

$$\varphi(s) = \frac{1}{2}\left(\frac{\|\boldsymbol{A}-\boldsymbol{A}^*\|^2}{\|\boldsymbol{A}^*\|^2} + \frac{\|\boldsymbol{C}-\boldsymbol{C}^*\|^2}{\|\boldsymbol{C}^*\|^2}\right) \tag{6.1}$$

Here, $\|\cdot\|$ is the Frobenius-norm and $\{\boldsymbol{A}^*, \boldsymbol{C}^*\}$ are the *target* values of the homogenized coefficient tensors $\{\boldsymbol{A}, \boldsymbol{C}\}$. To have the average or mean of the optimum texture to comply with the input mean height h_0, the following constraint is employed:

$$\chi(s) = \frac{(\langle h \rangle - h_0)^2}{h_0^2} \tag{6.2}$$

Whenever this constraint is satisfied, the definition of the film thickness ensures that

$$\langle \rho^\eta \rangle = \frac{h_0 - h_{\min}}{h_{\max} - h_{\min}} \tag{6.3}$$

is also satisfied for the design variables. There is also a constraint on the minimum and maximum values of the design variable which should remain in interval [0, 1]. Finally, the optimization problem for micro-texture reconstruction is formulated as

$$\textit{minimize } \varphi(s), \textit{ subject to } \chi(s) = 0 \textit{ and } s \in [0,1] \quad . \tag{6.4}$$

In this work, *method of moving asymptotes (MMA)* is employed as an optimization algorithm. This is a gradient-based algorithm first introduced in 1989 by K. Svanberg and revised in 2001. This algorithm requires taking sensitivities of the objective and the constraints with respect to design variables s^I for the optimization purpose.

6.2 Sensitivity Analysis

The sensitivity analysis of the objective function (6.1) is required, it contains the terms $\frac{\partial \boldsymbol{A}}{\partial s^I}$ and $\frac{\partial \boldsymbol{C}}{\partial s^I}$. The sensitivity analysis is carried out according to the discussion in [44]. It is an direct analytical sensitivity which is derived because of its computational efficiency and accuracy. For compactness, the terms

$$a = \frac{h^3}{12\mu} \quad , \quad b = \frac{h}{2} \tag{6.5}$$

are defined. The sensitivity analysis of $\boldsymbol{A}$ (the Poiseuille) and $\boldsymbol{C}$ (the Coutte) terms are as follows.

6.2.1 Poiseuille Term

The sensitivity of $\boldsymbol{A}$ follows from (4.26):

$$\frac{\partial A_{ij}}{\partial s^I} = \left\langle \frac{\partial a}{\partial s^I}(\delta_{ij} + \lambda_i^j) + a\frac{\partial \lambda_i^j}{\partial s^I} \right\rangle \quad . \tag{6.6}$$

For calculating the term $\frac{\partial \lambda_i^j}{\partial s^I}$, the cell problem of (4.21) will be utilized. Its weak form with the test function ϕ can be written as

$$\left\langle a\lambda_k^i \frac{\partial \phi}{\partial y_k} \right\rangle = -\left\langle a\frac{\partial \phi}{\partial y_i} \right\rangle \tag{6.7}$$

$\phi = \frac{\partial \omega^j}{\partial s^I}$ will be chosen and the following equation will be obtained

$$\left\langle a\frac{\partial \lambda_i^j}{\partial s^I} \right\rangle = -\left\langle a\lambda_k^i \frac{\partial \lambda_k^j}{\partial s^I} \right\rangle \quad . \tag{6.8}$$

Now, the right hand side of the above equation requires taking sensitivity of the cell problems itself with respect to s^I

$$\frac{\partial}{\partial y_k}\left(\frac{\partial a}{\partial s^I}\lambda_k^j + a\frac{\partial \lambda_k^j}{\partial s^I} \right) = -\frac{\partial}{\partial y_j}\left(\frac{\partial a}{\partial s^I} \right) \tag{6.9}$$

The weak form of the above expression with a test function π can be written as

$$\left\langle \frac{\partial a}{\partial s^I}\lambda_k^j \frac{\partial \pi}{\partial y_k} + a\frac{\partial \lambda_k^j}{\partial s^I}\frac{\partial \pi}{\partial y_k} \right\rangle = -\left\langle \frac{\partial a}{\partial s^I}\frac{\partial \pi}{\partial y_j} \right\rangle \tag{6.10}$$

Now, carefully selecting the test function $\pi = \omega^i$ one obtains an expression for the right-hand side of (6.8):

$$-\left\langle a\lambda_k^i \frac{\partial \lambda_k^j}{\partial s^I} \right\rangle = \left\langle \frac{\partial a}{\partial s^I}\lambda_k^j \lambda_k^i + \frac{\partial a}{\partial s^I}\lambda_j^i \right\rangle \quad . \tag{6.11}$$

Substituting this result in equation 6.6 and rearranging one obtains

$$\frac{\partial A_{ij}}{\partial s^I} = \left\langle \frac{\partial a}{\partial s^I}(\delta_{ik} + \lambda_k^i)(\delta_{jk} + \lambda_k^j) \right\rangle \quad . \tag{6.12}$$

This sensitivity analysis is similar to the one shown in [44] for linear elasticity and thermal conduction. This standard formulation is very important because this creates a basis for the sensitivity analysis of the tensor $\boldsymbol{C}$. At this point, it should be noted that one can easily show the tensor $\boldsymbol{A}$ can be written as

$$A_{ij} = \left\langle a(\delta_{ik} + \lambda_k^i)(\delta_{jk} + \lambda_k^j) \right\rangle \tag{6.13}$$

6.2.2 Couette Term

Taking sensitivity of tensor $\boldsymbol{C}$ with respect to design variables s^I delivers

$$\frac{\partial C_{ij}}{\partial s^I} = \left\langle \frac{\partial b}{\partial s^I}\delta_{ij} + \frac{\partial a}{\partial s^I}\Lambda_i^j + a\frac{\partial \Lambda_i^j}{\partial s^I} \right\rangle \tag{6.14}$$

Here, $\frac{\partial \Lambda_i^j}{\partial s^I}$ has to be calculated. Again going back to the cell problems (4.21) and taking the weak form into account and selecting $\phi = \frac{\partial \Omega^j}{\partial s^I}$ one obtains

$$\left\langle a\frac{\partial \Lambda_i^j}{\partial s^I} \right\rangle = -\left\langle a\lambda_k^i \frac{\partial \Lambda_k^j}{\partial s^I} \right\rangle \tag{6.15}$$

The right hand side is evaluated by taking the sensitivity of the cell problem (4.30) for Λ_k^i:

$$\frac{\partial}{\partial y_k}\left(\frac{\partial a}{\partial s^I}\Lambda_k^j + a\frac{\partial \Lambda_k^j}{\partial s^I} \right) = -\frac{\partial}{\partial y_j}\left(\frac{\partial b}{\partial s^I} \right) \quad . \tag{6.16}$$

The weak form of the above expression can be written by using a test function π as

$$\left\langle \frac{\partial \pi}{\partial y_k}\frac{\partial a}{\partial s^I}\Lambda_k^j + \frac{\partial \pi}{\partial y_k} a\frac{\partial \Lambda_k^j}{\partial s^I} \right\rangle = -\left\langle \frac{\partial \pi}{\partial y_j}\frac{\partial b}{\partial s^I} \right\rangle \tag{6.17}$$

The right hand side of (6.15))is obtained by choosing $\pi = \omega^i$ as

$$-\left\langle a\lambda^i_k \frac{\partial \Lambda^j_k}{\partial s^I} \right\rangle = \left\langle \lambda^i_k \frac{\partial a}{\partial s^I}\Lambda^j_k + \lambda^i_j \frac{\partial b}{\partial s^I} \right\rangle \tag{6.18}$$

Now, substituting this result in (6.14) and rearranging, one obtains the sensitivity expression:

$$\frac{\partial C_{ij}}{\partial s^I} = \left\langle \frac{\partial b}{\partial s^I}(\delta_{ij} + \lambda^i_j) + \frac{\partial a}{\partial s^I}(\Lambda^j_i + \lambda^i_k \Lambda^j_k) \right\rangle \quad . \tag{6.19}$$

Following (6.13) one can also write an alternative form of the tensor $\boldsymbol{C}$ as follows

$$C_{ij} = \left\langle b(\delta_{ij} + \lambda^i_j) + a(\Lambda^j_i + \lambda^i_k \Lambda^j_k) \right\rangle \quad . \tag{6.20}$$

This sensitivity analysis of homogenized coefficients appears both in MicOO and MacOO settings. The filtering which was introduced in (Section 5.1) also has an influence on the sensitivity analysis. Referring to the texture design one can write the following expression for the sensitivity $\left\langle \frac{\partial \mathcal{H}(h)}{\partial s^I} \right\rangle$ of any arbitrary function $\mathcal{H}$ as

$$\begin{aligned}
\left\langle \frac{\partial \mathcal{H}(h)}{\partial s^I} \right\rangle &= \left\langle \frac{\partial \mathcal{H}}{\partial h}\frac{\partial h}{\partial \rho} \sum_K \frac{\partial \rho}{\partial \rho^K}\frac{\partial \rho^K}{\partial s^I} \right\rangle = \\
&\left\langle \frac{\partial \mathcal{H}}{\partial h}\{\eta(h_{\max} - h_{\min})\rho^{\eta-1}\} \sum_K N^K \frac{\partial \rho^K}{\partial s^I} \right\rangle \\
&= \frac{1}{|\mathcal{Y}|}\sum_K \int_{\mathcal{Y}^K} \left(\frac{\partial \mathcal{H}}{\partial h}\{\eta(h_{\max} - h_{\min})\rho^{\eta-1}\} N^K \frac{\partial \rho^K}{\partial s^I} \right) \mathrm{d}a
\end{aligned} \tag{6.21}$$

Here, $\mathcal{Y}^K \subset \mathcal{Y}$ indicates the span of N^K. When ρ is element-wise constant, K indexes the elements and $N^K = 1$ only within the domain of its element.

6.3 Numerical Examples

By micro-texture reconstruction one can asses the credibility of the optimization algorithm numerically as well as visually. Along with the numerical assessment visual assessment is important as well to evaluate the desired feature size. It can also be used to see whether different micro-textures can output similar macroscopic response in terms of $\boldsymbol{A}$ and $\boldsymbol{C}$. Instead of trial and error approach to look for the desired macroscopic response for optimization one can generate it by inputing a micro-texture. For the tests of texture design, 0-OR-1 and 0-TO-1 textures were designed for Q1S0 and Q1S1 element types. The optimization process is checked for both macroscopically *isotropic* and *anisotropic* responses. The height parameters for the target micro-textures are $h_{min} = 0.1\mu m$ and $h_{max} = 3\mu m$. The viscosity of the fluid is $\mu = 0.14 Pa.s$. According to the visualization schemes (see Fig. 5.2) the target textures along with there target macroscopic responses $\boldsymbol{A}^*, \boldsymbol{C}^*, h_0$ and the corresponding homogeneous responses are summarized in Appendix B. The units are μm for $\{h_0, \boldsymbol{C}\}$ and $\mu\text{m}^3/\text{Pa}\cdot\text{s}$ for $\boldsymbol{A}$. In order to additionally assess the influence of the texture, the macroscopic response of the homogeneous interface with $h = h_0$ is also reported via the quantities

$$\left[A_0\right] = \begin{bmatrix} \frac{h_0^3}{12\mu} & 0 \\ 0 & \frac{h_0^3}{12\mu} \end{bmatrix} \quad , \quad \left[C_0\right] = \begin{bmatrix} \frac{h_0}{2} & 0 \\ 0 & \frac{h_0}{2} \end{bmatrix} \quad . \tag{6.22}$$

Note that, depending on the particular texture, the magnitude of $\boldsymbol{A}^*$ may be larger or smaller with respect to $\boldsymbol{A}_0$, indicating that the texture can facilitate or hinder macroscopic fluid flux due to a pressure gradient. On the other hand, the magnitude of $\boldsymbol{C}^*$ is always less than the magnitude of $\boldsymbol{C}_0$. This is due to the fact that, in the specialized setup of CASE 1 that is representative of alternate scenarios, the stationary rough surface holds fluid back from being dragged along with the moving upper surface, i.e. $\overline{\boldsymbol{B}}$ has predominantly negative entries.

6.4 Default Numerical Choices

For 0-OR-1 design $\eta = 3$ and for 0-TO-1 $\eta = 1$ is selected. All the parameters in the MMA algorithm is kept the same as provided [2] except for the move limit parameter `move` in `mmasub.m` which is set to be at 0.1 instead of 1.0 to have a smoother convergence of the optimization algorithm in terms of the variation of the objective function through the iterations. To set the convergence (or so-called stop criteria for the optimization process) one can set a limit for (6.1) and (6.2). The tolerance on the objective φ is set to be at $\text{TOL}_{\varphi} = 10^{-3}$ and tolerance on the constraint χ is set at $\text{TOL}_{\chi} = 10^{-4}$, which is a little more strict to comply the mean film thickness of the designed texture to the macroscopic mean film thickness as close as possible to have minimum error possible in the macroscopic response. So, if φ and χ go below these two value at the same optimization iteration then the optimization is stopped. It was observed that the tolerance on the constraint is achieved much faster compared to the objective hence the objective asserts a high computational cost during the optimization process. The objective (6.1) is slightly modified to make the optimization process faster by modifying it to to $\varphi' = 100\varphi + 1$ so that its value always remains in between 1 and 100, which is more favorable for use in MMA. Hence, so the corresponding tolerance becomes $\text{TOL}_{\varphi'} = 1.1$. The microscopic optimization is carried out on a square unit cell $\mathcal{Y}$ which has a side length $L = 10\mu m$. This unit cell is discretized with a mesh of $N \times N$ elements with either Q1S1 or Q1S0 element type. It should be mentioned here that the frequency of the oscillation does not have any effect on the macroscopic result in the context of homogenization based on the Reynolds equation. Optimization parameters like initial guess, filter type and filter radius etc., are selected through numerical examples. Default choices to be identified will be used in further optimization problems as selected unless otherwise stated.

6.5 Initial Guess

The optimization process is dependent on the initial guess. Three different initial guesses were tested. In the first initial guess a s_0 distribution is obtained such that $h = h_0$ and the value of s is perturbed by $1 - s_0$, except that if s_0 is equal to 0.5 then it is perturbed as $1 - s_0 + \delta$, at the coordinates $(N/2, N/2)$. The second initial guess is the uniformly distributed s and the third initial guess is the random $s-$distribution generated from a Gaussian random number generator. Here, the comparison is made on the basis of the number of iterations to converge to the desired tolerances on the objective and the constraint and as well as through a visual assessment. Four cases were run for both 0-OR-1 and 0-TO-1 texture example. For a 0-OR-1 design a trapezoidal hole texture was selected and for a 0-TO-1 design a circular bump texture was selected. It is clear from the

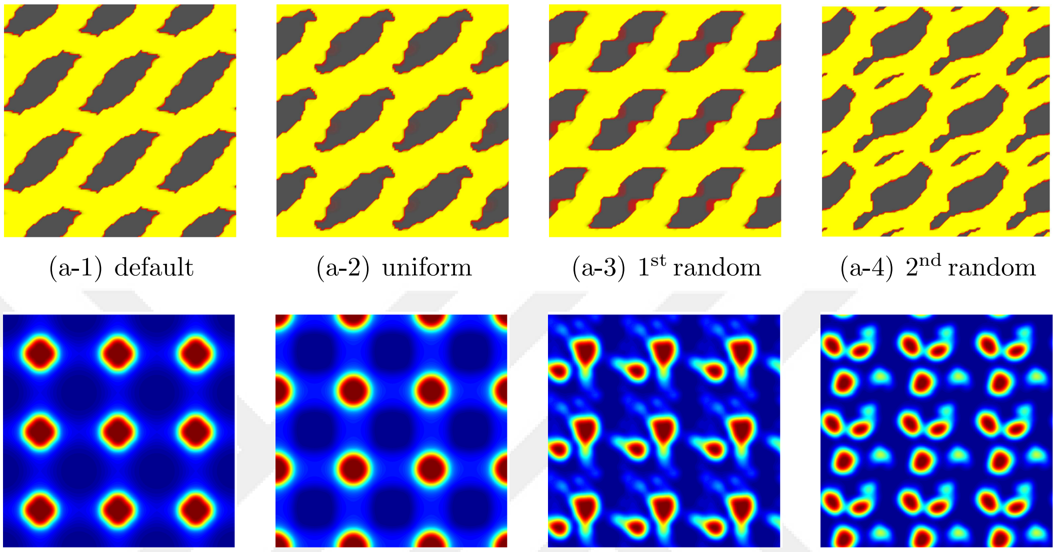

(a-1) default (a-2) uniform (a-3) 1st random (a-4) 2nd random

(b-1) default (b-2) uniform (b-3) 1st random (b-4) 2nd random

Figure 6.1: *Influence of the initial guess is demonstrated using (a)* 0-OR-1 *type trapezoidal hole texture and (b)* 0-TO-1 *type circular bump texture. The number of iterations to convergence were (a)* $\{216, 529, 310, 1087\}$ *and (b)* $\{78, 959, 103, 93\}$.

results (see Fig. 6.1) that the least number of iterations and visually appealing textures were obtained with the perturbed s_0 distribution from the middle while the uniform s_0 distribution shows higher number of iterations to converge and random distribution shows similar trend along with a very different texture from the input micro-texture which is contrary to the micro-texture reconstruction. The fact that there are different optimum micro-textures is because of the well-known non-uniqueness present in the result due to the degree of freedom available of FEM mesh, reader is refered to [49] [50] and [51] for more detailed studies on non-uniqueness. So $1-s_0$ is selected as a default initial guess for all the numerical examples in this work.

6.6 Mesh Resolution and Filter Type

The resolution has an obvious effect on the macroscopic response and hence on the optimization process itself. Mesh resolution of $N = 40$ is satisfactory and delivers textures comparable with higher mesh resolution (see Figure 6.2). Note that the filter radius was scaled with increasing mesh resolution in order to preserve the feature size. The diagonal groove texture is selected for 0-OR-1 test and diagonal wave texture is selected for 0-TO-1 test.

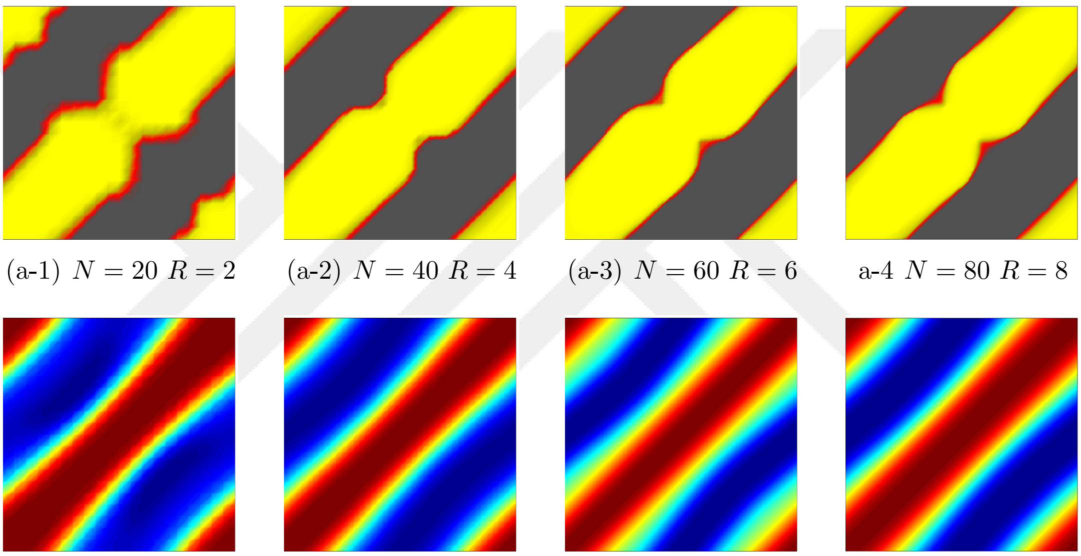

(a-1) $N = 20$ $R = 2$ (a-2) $N = 40$ $R = 4$ (a-3) $N = 60$ $R = 6$ a-4 $N = 80$ $R = 8$

(b-1) $N = 20$ $R = 2$ (b-2) $N = 40$ $R = 4$ (b-3) $N = 60$ $R = 6$ (b-4) $N = 80$ $R = 8$

Figure 6.2: *The rapid convergence with increasing mesh resolution is demonstrated (default:* $N = 40$*) using the diagonal textures. (a)* 0-OR-1 *Diagonal groove texture. (b)* 0-OR-1 *Diagonal wave texture. The number of iterations to convergence were (a)* $\{45, 8, 8, 9\}$ *and (b)* $\{24, 15, 28, 36\}$.

Similar to the mesh resolution, the erode and dilate type filters in Table 5.1 which are suitable for 0-OR-1 design were observed to only weakly influence the output design (Figure 6.3). However, the particular choice strongly influences the number of iterations to convergence. In particular, geometric erode delivers smoother edges but at a relatively high cost. In all cases, the default exponential erode filter was observed to deliver rapid convergence. So, exponential erode filter is selected for 0-OR-1 design which results in better designs in a smaller number of iterations. For 0-TO-1 design linear density filter was employed because all the other erode or dilate are designed to deliver a 0-OR-1 texture.

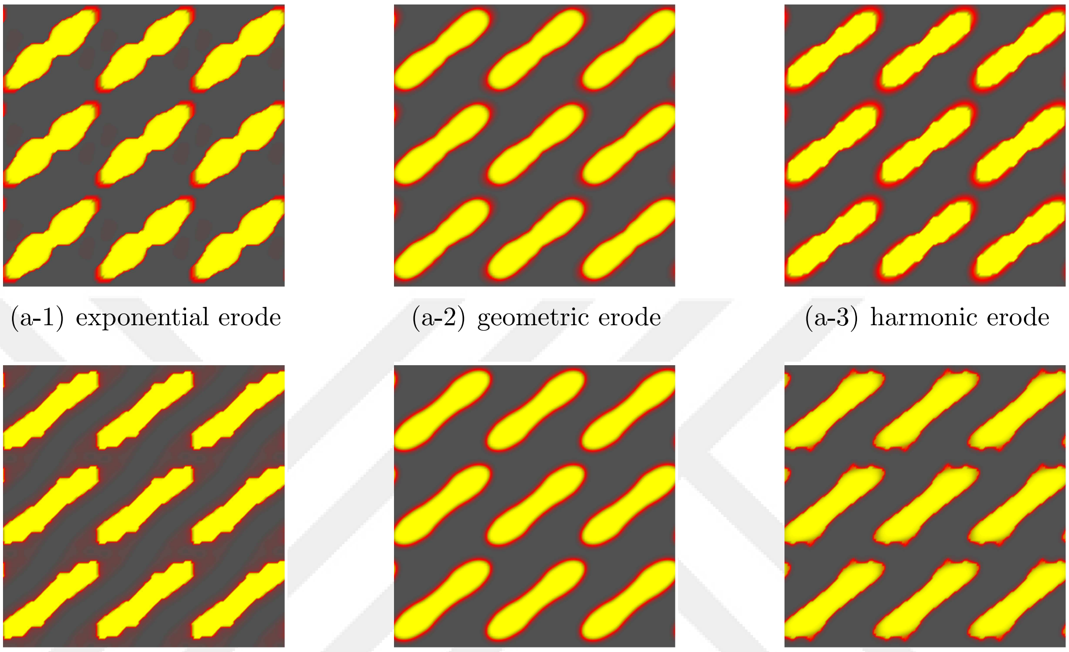

(a-1) exponential erode (a-2) geometric erode (a-3) harmonic erode

(b-1) exponential dilate (b-2) geometric dilate (b-3) harmonic dilate

Figure 6.3: *Influence of the (a) erode and (b) dilate type filters is depicted using the* 0-OR-1 *trapezoidal pillar texture. The number of iterations to convergence were (a)* $\{21, 66, 50\}$ *and (b)* $\{106, 101, 63\}$.

6.7 Filter Radius and Element Type

Filter radius provides the feature size and also affects the convergence. For instance, if the filter radius is too small the feature size of the desired texture will be very small and if it is too large then it will effect the convergence and the number of iterations will increase. For both Q1S0 and Q1S1 element types, the default filter radius i.e. $N/10 = 4$ is suitable. It can also be observed (see Fig. 6.4 and 6.5) that Q1S1 element type provides better results without filtering as compared to Q1S0 element type and it is less prone to numerical instabilities such as checker-boards. On the other hand, after selecting a suitable filter radius, both Q1S1 and Q1S0 are mutually interchangeable. Element type Q1S0 can be used with a reasonable filter radius considering the significantly less computational expense.

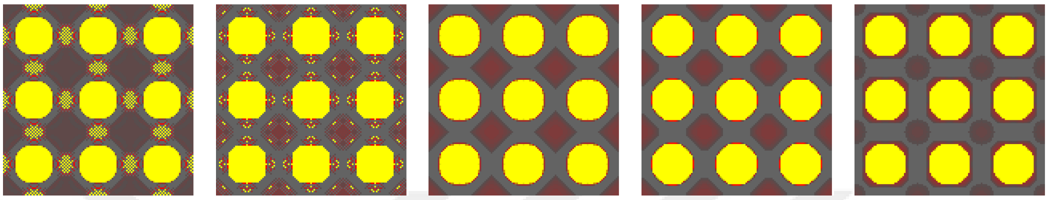

(a-1) no filter (a-2) $R = 1$ (a-3) $R = 2$ (a-4) $R = 4$ (a-5) $R = 8$

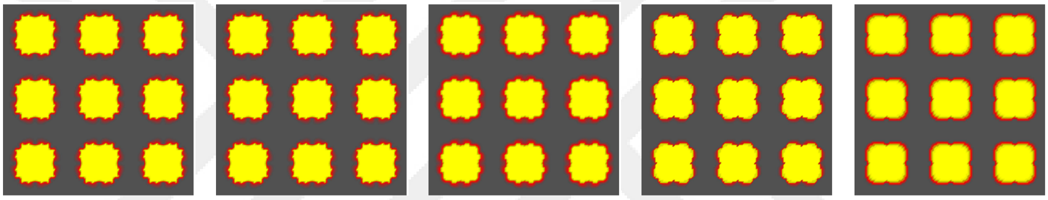

(b-1) no filter (b-2) $R = 1$ (b-3) $R = 2$ (b-4) $R = 4$ (b-5) $R = 8$

Figure 6.4: *The effect of the element type (default: Q1S1) and filtering (default: $R = 4$) is demonstrated for* 0-OR-1 *type circular pillar texture from Figure 6.6 for (a) Q1S0 and (b) Q1S1 elements. The number of iterations to convergence were (a)* $\{148, 125, 122, 145, 159\}$ *and (b)* $\{110, 110, 93, 93, 229\}$.

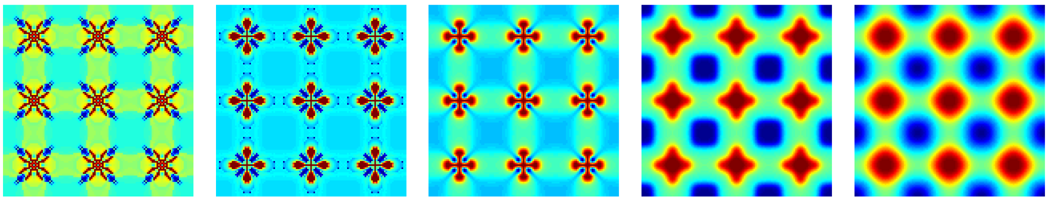

(a-1) no filter (a-2) $R = 1$ (a-3) $R = 2$ (a-4) $R = 4$ (a-5) $R = 8$

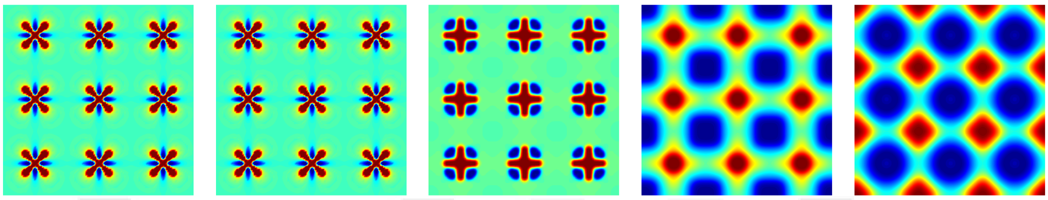

(b-1) no filter (b-2) $R = 1$ (b-3) $R = 2$ (b-4) $R = 4$ (b-5) $R = 8$

Figure 6.5: *The effect of the element type (default: Q1S1) and filtering (default: $R = 4$) is demonstrated for* 0-TO-1 *type sinusoidal texture from Figure 6.8 for (a) Q1S0 and (b) Q1S1 elements. The number of iterations to convergence were (a)* $\{80, 103, 85, 73, 107\}$ *and (b)* $\{79, 79, 144, 76, 116\}$.

After selecting the default numerical choices and the optimization parameters, the optimization for the reconstruction of default textures from Appendix B are shown in the following figures.

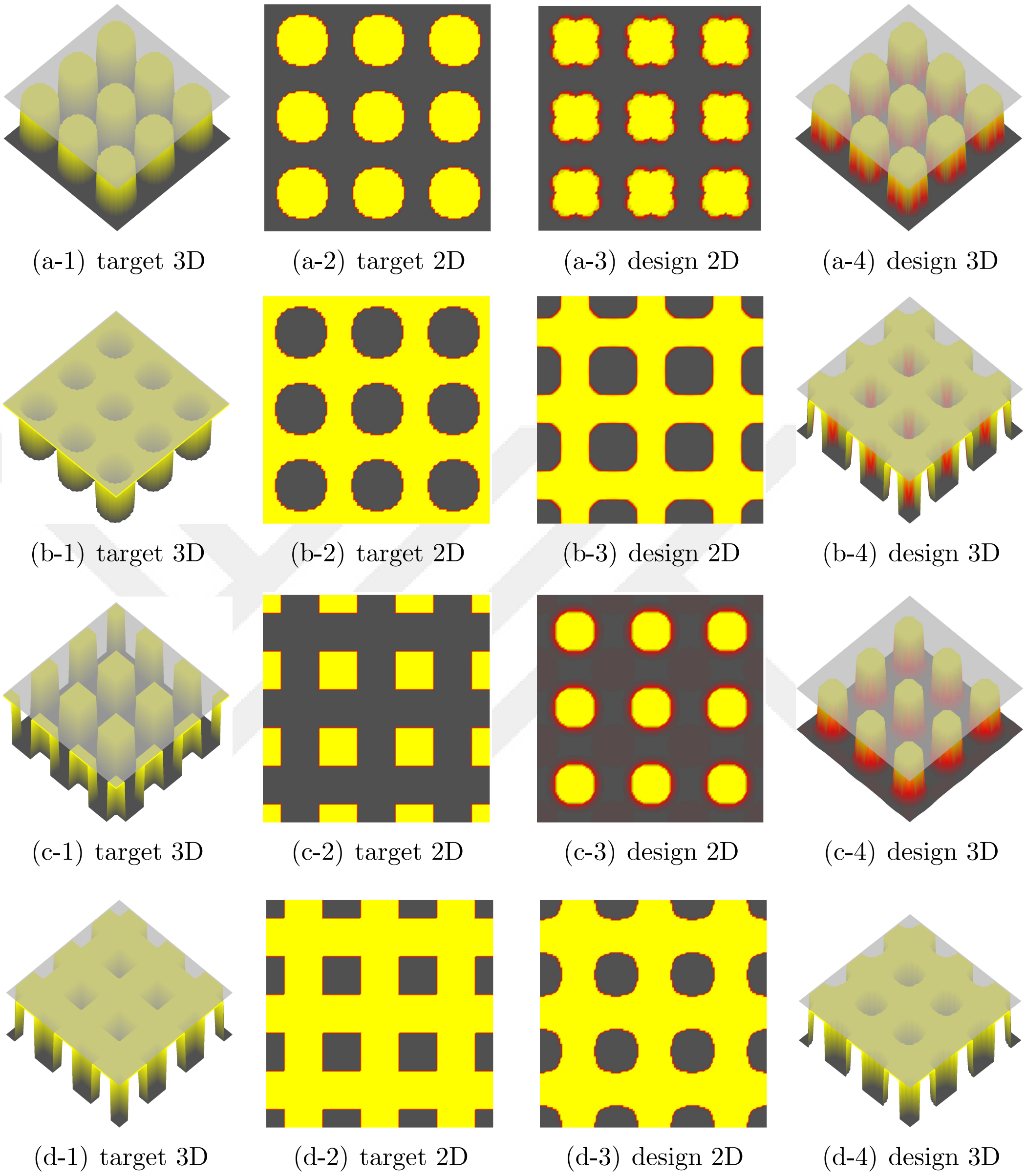

Figure 6.6: *Benchmark target textures of the* 0-OR-1 *type displaying a macroscopically isotropic response are depicted together with the output designs from the optimization algorithm based on the default numerical choices. The number of iterations to convergence were (a)* 93 *for the circular pillar texture, (b)* 47 *for the circular hole texture, (c)* 82 *for the square pillar texture, and (d)* 93 *for the square hole texture. see Table B.1 in Appendix B for corresponding target responses.*

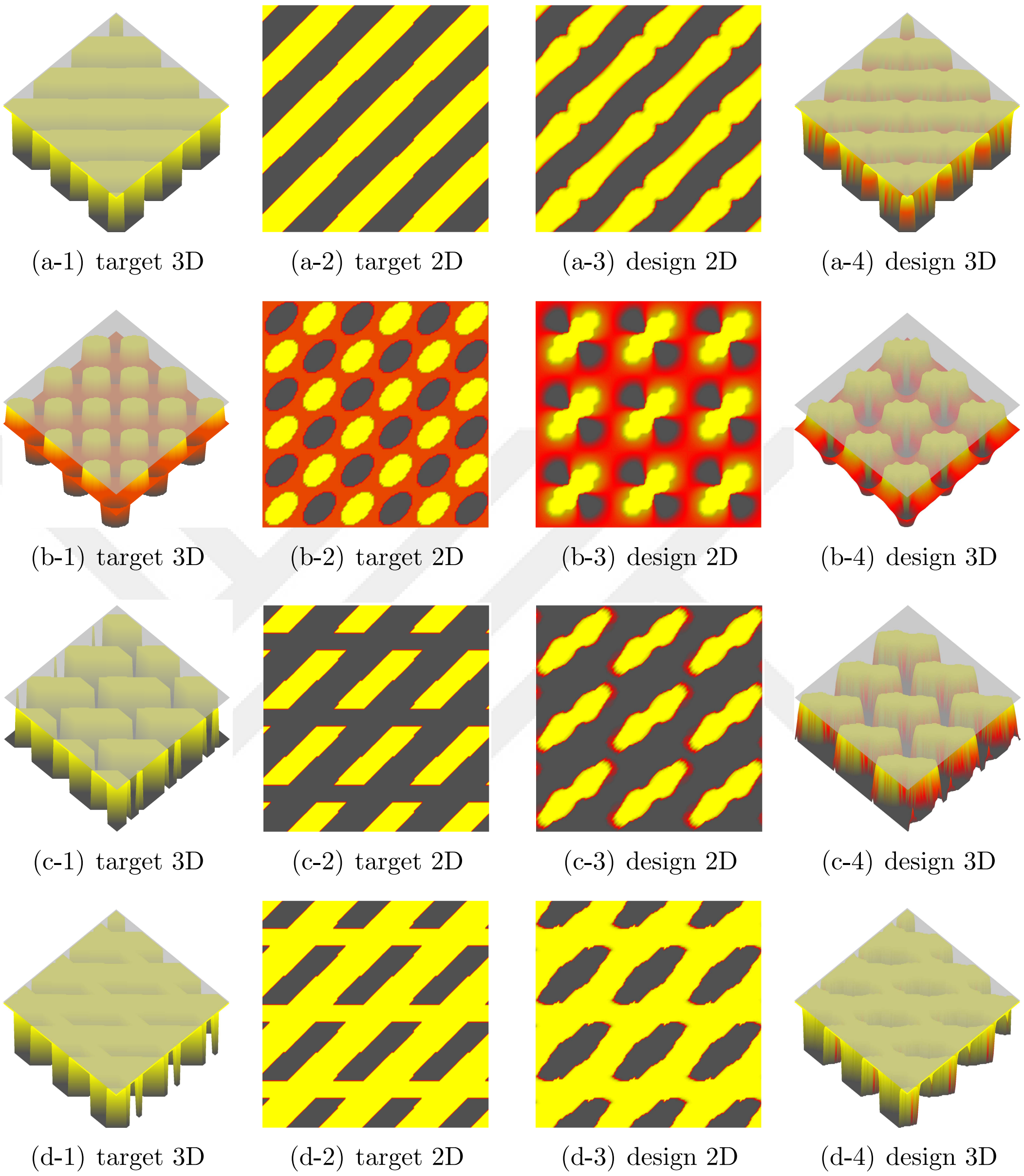

Figure 6.7: *Benchmark target textures of the* 0-OR-1 *type displaying a macroscopically isotropic response are depicted together with the output designs from the optimization algorithm based on the default numerical choices. The number of iterations to convergence were (a)* 8 *for the diagonal groove texture, (b)* 75 *for the ellipsoidal texture with alternating pillars and holes, (c)* 21 *for the trapezoidal pillar texture, and (d)* 216 *for the trapezoidal hole texture. see Table B.2 in Appendix B for corresponding target responses.*

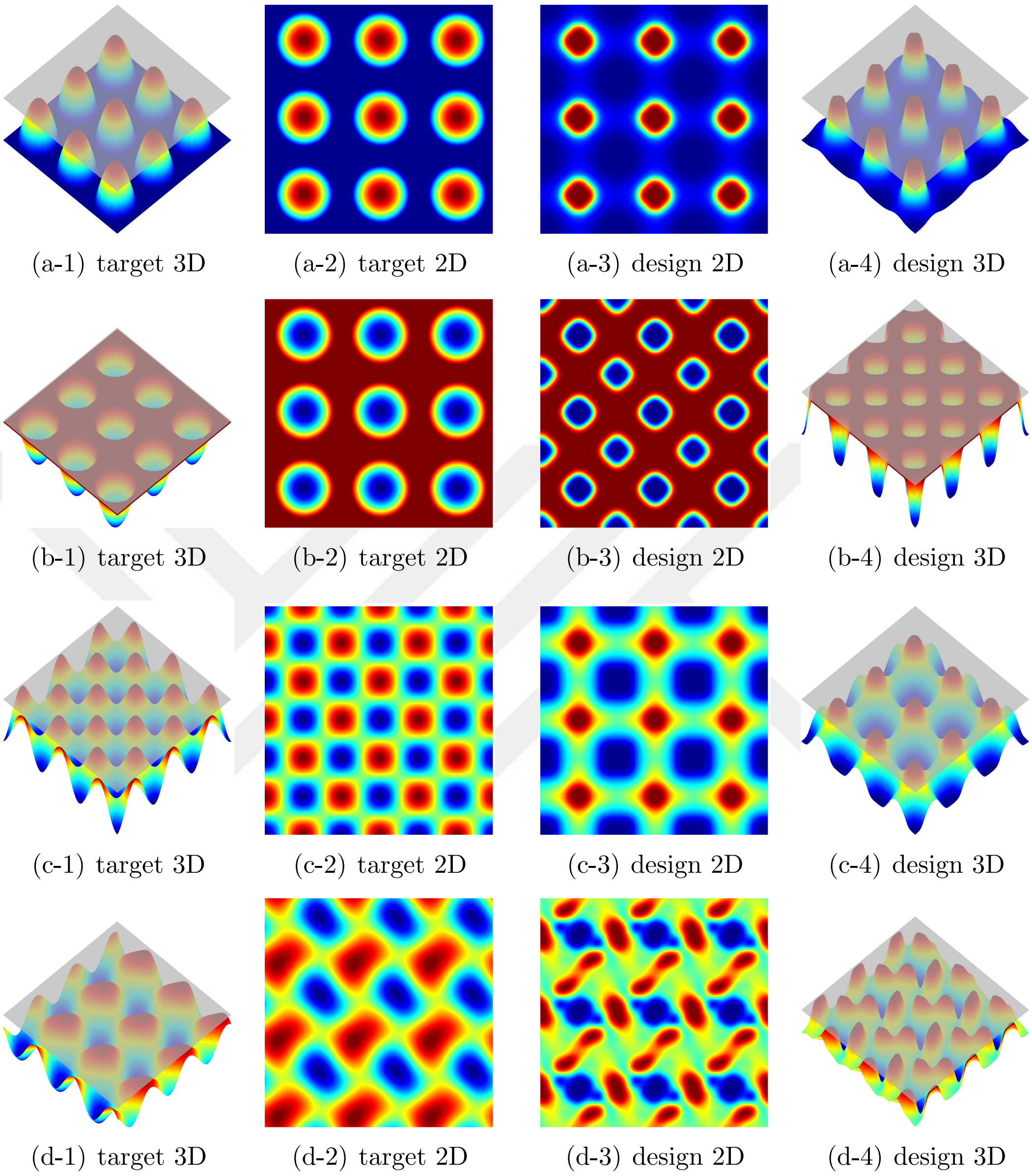

Figure 6.8: *Benchmark target textures of the* 0-TO-1 *type displaying a macroscopically* <u>*isotropic*</u> *response are depicted together with the output designs from the optimization algorithm based on the default numerical choices. The number of iterations to convergence were (a)* 78 *for the circular bump texture, (b)* 41 *for the circular dimple texture, (c)* 76 *for the sinusoidal texture, and (d)* 127 *for the distorted sinusoidal texture. see Table B.3 in Appendix B for corresponding target responses. Note that the last texture is relatively weakly an-isotropic and hence included in this list.*

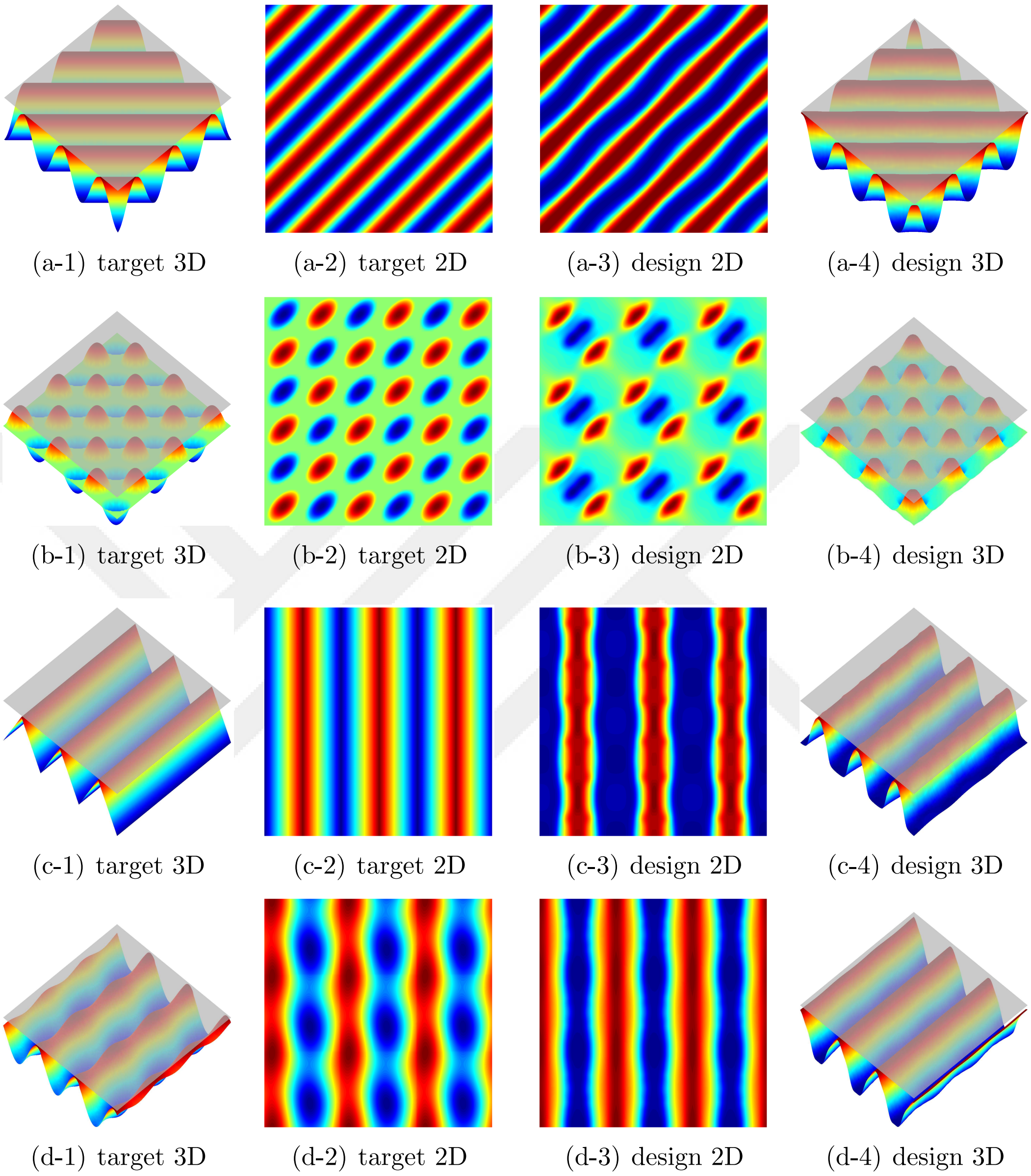

(a-1) target 3D (a-2) target 2D (a-3) design 2D (a-4) design 3D

(b-1) target 3D (b-2) target 2D (b-3) design 2D (b-4) design 3D

(c-1) target 3D (c-2) target 2D (c-3) design 2D (c-4) design 3D

(d-1) target 3D (d-2) target 2D (d-3) design 2D (d-4) design 3D

Figure 6.9: *Benchmark target textures of the* 0-TO-1 *type displaying a macroscopically anisotropic response are depicted together with the output designs from the optimization algorithm based on the default numerical choices. The number of iterations to convergence were (a)* 15 *for the diagonal wave texture, (b)* 115 *for the ellipsoidal texture with alternating bumps and dimples, (c)* 29 *for the triangular groove texture, and (d)* 41 *for the wavy groove texture. see Table B.4 in Appendix B for corresponding target responses.*

6.8 Onsager's Principle

All the micro-textures considered in the reconstruction delivers symmetric homogenized coefficients $\boldsymbol{A}$ and $\boldsymbol{C}$. The tensor $\boldsymbol{A}$ is always symmetric and positive-definite [52]. It obeys Onsager's principle but there is no such restriction for $\boldsymbol{C}$, which can also be observed in thermoelectricity and is defined by Seedbeck and Peltier effects. Textures with non-symmetric $\boldsymbol{C}$ tensors may be designed using this fact. This can be done by removing the first term from φ in (6.1). For a 0-OR-1 example, h_0 was prescribed closer to h^- than h^+, which is expected to lead to holes on the surface rather than pillars. For a 0-TO-1 example, a mediocre h_0 value was prescribed which is expected to lead to a smoothly varying texture. Appropriate sample input values, found by trial and error, are (in μm):

$$\begin{aligned}
&\underline{\text{0-OR-1 :}} \quad h_0 = 0.80 \quad , \quad \left[C^*\right] = \begin{bmatrix} 0.10 & 0.10 \\ 0.00 & 0.05 \end{bmatrix} \quad , \\
&\underline{\text{0-TO-1 :}} \quad h_0 = 1.45 \quad , \quad \left[C^*\right] = \begin{bmatrix} 0.30 & 0.20 \\ 0.10 & 0.40 \end{bmatrix} \quad .
\end{aligned} \tag{6.23}$$

The corresponding designs are depicted in Figure 6.10, which verify the previous assertion regarding the existence of such textures.

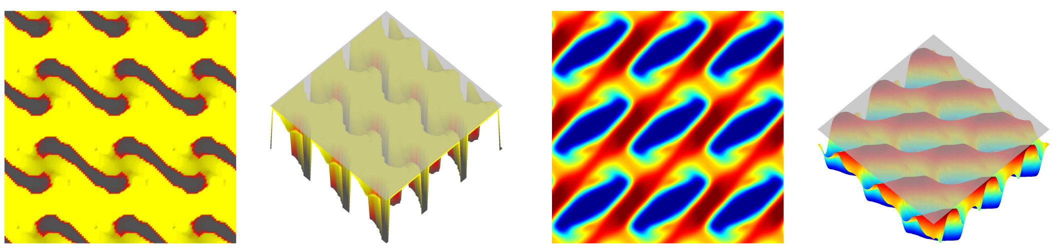

(a-1) 0-OR-1 : 2D (a-2) 3D (b-1) 0-TO-1 : 2D (b-2) 3D

Figure 6.10: *(a)* 0-OR-1 *type design and (b)* 0-TO-1 *type design — see Table B.5 in Appendix B for corresponding macroscopic responses. The number of iterations to convergence were (a)* 229 *and (b)* 44.

6.9 Sensitivity Validation

To validate the analytic sensitivities evaluated in Section 6.2, see Fig. 6.11, the sensitivity of the objective function (6.1) is calculated with respect to design variables i.e., $\partial\varphi/\partial s^I$, for both Q1S1 and Q1S0 element types and compared with the numerical counterparts. These sensitivities are for the converged textures, at the last iteration of the optimization. The sensitivity of a 0-OR-1 and 0-TO-1 texture is calculated and presented in the top row while the difference between the second order numerical sensitivity, with 10^{-4} for s^I perturbation, and analytic sensitivities are shown in the second row.

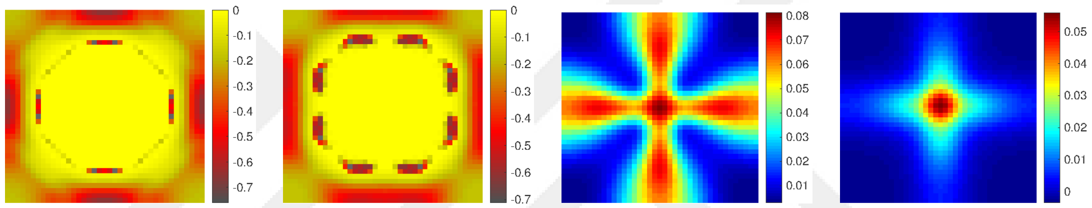

(a-1) $Q1S0$: analytical (a-2) $Q1S1$: analytical (a-3) $Q1S0$: analytical (a-4) $Q1S1$: analytical

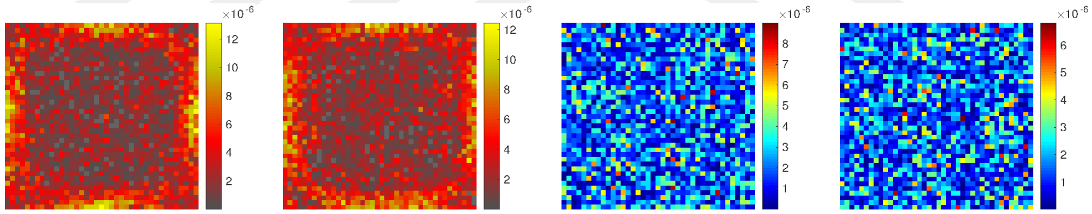

(b-1) $Q1S0$: numerical (b-2) $Q1S1$: numerical (b-3) $Q1S0$: numerical (b-4) $Q1S1$: numerical

Figure 6.11: *Analytical and numerical sensitivity distributions $\partial\varphi/\partial s^I$ are compared on converged* 0-OR-1 *and* 0-TO-1 *type textures from figures 6.4 and 6.5 for both $Q1S0$ and $Q1S1$ elements ($R = 4$).*

Chapter 7

Macroscale Objective Optimization

In this chapter, first two different macroscopic HDL problems are introduced: *squeeze film flow* and *wedge problem*. Three different objective formulations introduced earlier were tested for squeeze film flow and one case that is specifically relevant for the wedge problem. Finally, optimization with Taylor's approximation is introduced considering the computational expense of a full two-scale approach.

7.1 Squeeze Film Flow

MacOO can be formulated for different lubricating problems for instance hard disk slider head, squeeze film flow, bearing of a car, prosthetic joints and wedge problem etc. Here optimization for two of these applications will be discussed: squeeze film flow and wedge problem. A positive pressure is generated if two plates are moving towards each other. The fluid present will take some finite amount of time to squeeze out of the plates and this is the cause of cushioning effect in the squeeze film flow. A negative pressure which might cause cavitation is produced when the plates move apart from each other. This type of fluid flow is used mostly in dampers and shock absorbers. The schematic of squeeze film flow is shown in Fig. (7.1) in 1D, the lower plate is rough and stationary and the upper plates moves between a maximum ($h_{0_{max}} = 1.0\mu m$ and $h_{0_{min}} = 2.5\mu m$) mean fluid film thickness with vertical velocity of

$$\frac{\partial h_0}{\partial t} = v_0 sin(T\pi) \tag{7.1}$$

Here, $v_0 = \pm 1\mu m/s$, $-$ when the plates approach each other and $+$ when the upper plates move apart, and $T = 1s$. The velocity can be constant as well instead of a sine function but in that case very rapid transitions occur between the maximum pressure generated, when plates approach each other, and maximum cavitation generated, when plates apart from each other which is physically not entirely realistic. The homogenized equation for the squeeze film flow can be derived in the same fashion as in Chapter 4 for Reynolds equation. Here, the homogenized coefficients reduces to $\boldsymbol{A}$ only because there is no horizontal velocity present. Moreover, $\boldsymbol{A}$ can be evaluated only once for a h_0 position at a time step and utilized for all over the interface because the surfaces are parallel to each other which makes mean film thickness at an instance constant. This makes this problem computationally less expensive than the wedge problem when it has to be evaluated at every point because the h_0 is not constant in a wedge. The governing equation for squeeze film flow can be written as

$$-\nabla_{\boldsymbol{x}} \cdot (-\boldsymbol{A}(\boldsymbol{x})\nabla_x p_0(\boldsymbol{x})) = \frac{\partial h_0}{\partial t} \tag{7.2}$$

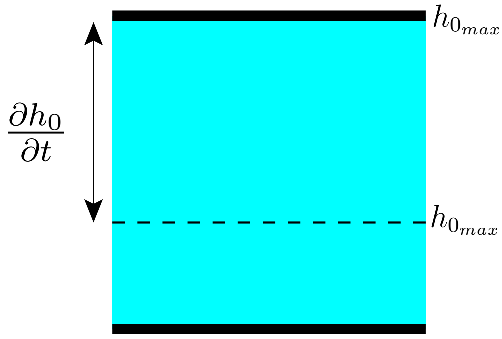

Figure 7.1: *Schematic of squeeze film flow.*

7.1.1 Micro Texture Reconstruction for MacOO

Again in MacOO to check the sanity of the optimization algorithm, the micro-texture reconstruction is conducted. The objective can be formulated using the pressure distribution. In this case, a target micro-texture is used to calculate the homogenized pressure response. This pressure response is fed into the optimization algorithm rather than the homogenized coefficients. This optimization can be done for a particular time step hence at a particular h_0 value to eradicate the extra computational cost associated with time integration over the whole squeeze film cycle and only focus on the credibility of the optimization problem. The objective can be formulated as

$$\varphi(s) = \frac{\int_\Omega (p_0^* - p_0(s))^2 d\Omega}{\int_\Omega (p_0^*)^2 d\Omega} \tag{7.3}$$

Here, p_0^* is the target pressure response which is generated by a target micro-texture and $p_0(s)$ is the pressure at current optimization iteration and it is dependent on the design variables which defines the texture. So, here the optimization algorithm will try to come up with a micro-texture which will reduce the difference between these two pressure distributions. The expression in the denominator (7.3) is used to scale the objective to comply it with the optimization algorithm. Here, all the numerical choices and optimization parameters are the same as the ones used in MicOO, along with the constraints, except that the default element type that is used in MacOO is Q1S0 because of the computational expense associated with Q1S1 element type. The minimum and maximum fluid film thickness at the microscale selected is $\bar{h}_{min} = -0.5$ and $\bar{h}_{max} = 0.5$. Here, from Eq. (4.4), $h = h_0 - \bar{h}$ due to lower rough surface. $\bar{h}$ can be written using (5.4)

$$\bar{h}(\rho) = \bar{h}_{min} + (\bar{h}_{max} - \bar{h}_{min})\rho^{\eta} \quad \in [\bar{h}_{min}, \bar{h}_{max}] \tag{7.4}$$

The final optimization problem will look like Eq. 6.4. The sensitivity of objective (7.3) contains the term $\frac{\partial p_0}{\partial s^I}$ which follows from taking the sensitivity of the macroscopic PDE (4.31). This can be written as

$$-\nabla_{\boldsymbol{x}} \cdot \left(-\frac{\partial \boldsymbol{A}}{\partial s^I} \nabla_{\boldsymbol{x}} p_0 - \boldsymbol{A} \nabla_{\boldsymbol{x}} \frac{\partial p_0}{\partial s^I} + \frac{\partial \boldsymbol{C}}{\partial s^I} \bar{\boldsymbol{U}} \right) = 0 \tag{7.5}$$

In (7.5) the first and the third terms are already known and can be calculated for every h_0. The only unknown is the $\frac{\partial p_0}{\partial s^I}$ which can be solved for each s^I. In MacOO, for the solution of macroscopic problems p_0 and $\partial p_0 / \partial s^I$, a mesh resolution of 20×20 is used. In the case of squeeze film flow, where there is no $\boldsymbol{C}\bar{\boldsymbol{U}}$ present, sensitivity reduces to

$$-\nabla_{\boldsymbol{x}} \cdot \left(-\frac{\partial \boldsymbol{A}}{\partial s^I} \nabla_{\boldsymbol{x}} p_0 - \boldsymbol{A} \nabla_{\boldsymbol{x}} \frac{\partial p_0}{\partial s^I} \right) = 0 \tag{7.6}$$

For micro-texture reconstruction for MacOO, one 0-or-1 and one 0-to-1 texture were reconstructed (see Fig. 7.2). In micro-texture reconstruction using macroscopic objective the non-uniqueness increases as can be observed by comparing the design texture in Fig. 6.7. This increase in non-uniqueness is because of the fact that there is more degree of freedom available for the design variable because of the indirect dependence of design variables s^I on p_0 through homogenized coefficient $\boldsymbol{A}$.

7.1.2 Micro Texture Optimization for Prescribed Load Bearing Capacity

Reconstructing the micro-textures gives confidence in the optimization algorithm and now one can try optimizing for a prescribed load bearing capacity using this

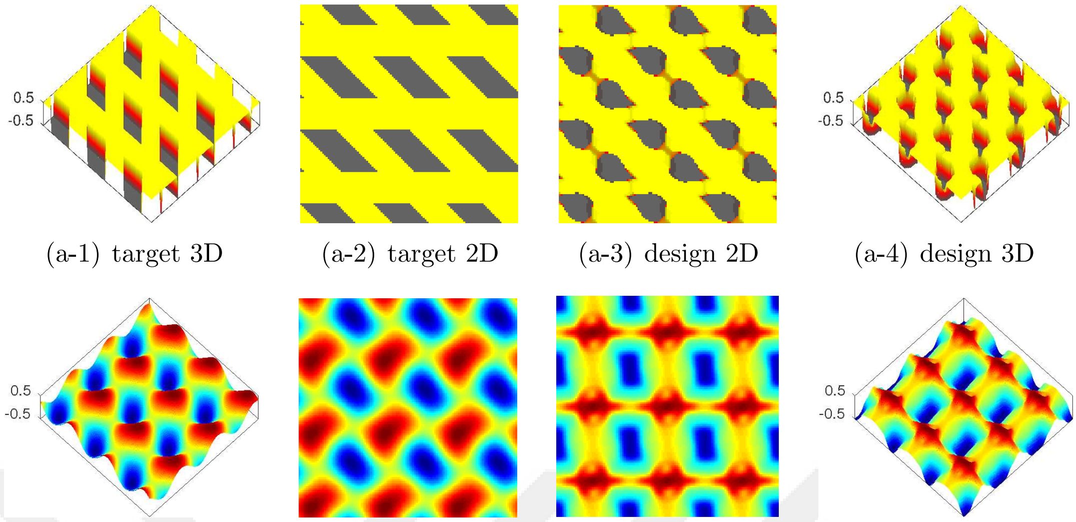

Figure 7.2: *Micro-texture reconstruction using macroscopic objective optimization (7.3). (a) Trapezoidal holes anisotropic* 0-OR-1 *design. (b) Distorted sinusoidal texture isotropic* 0-TO-1 *design.*

framework. The load bearing capacity L_0 is defined as the integral of pressure over the lubrication interface

$$L_0(s) = \int_\Omega p_0(s) d\Omega \tag{7.7}$$

The objective can be formulated as

$$\varphi(s) = \frac{(L_0^* - L_0(s))^2}{(L_0^*)^2} \tag{7.8}$$

Again in this optimization problem the objective is formulated at a particular time step and h_0, with $\frac{\partial h_0}{\partial t} = -1\mu m/s$. The height parameters are same i.e., $h_0 = 1\mu m$, $\bar{h}_{min} = -0.5$ and $\bar{h}_{max} = 0.5$. In the objective (7.8), L_0^* is defined by

$$L_0^* = l_f \times L_{hom} \tag{7.9}$$

Here, $L_{hom} = 94.1\mu N$ is the load bearing capacity at the homogeneous interface (h_0 without a surface roughness present) and l_f is so-called *load factor*. So, by adjusting the load factor l_f one can design different target load bearing capacities the optimization algorithm will deliver the corresponding micro-textures for those load factors. As the load bearing capacity increases the walls of the micro-

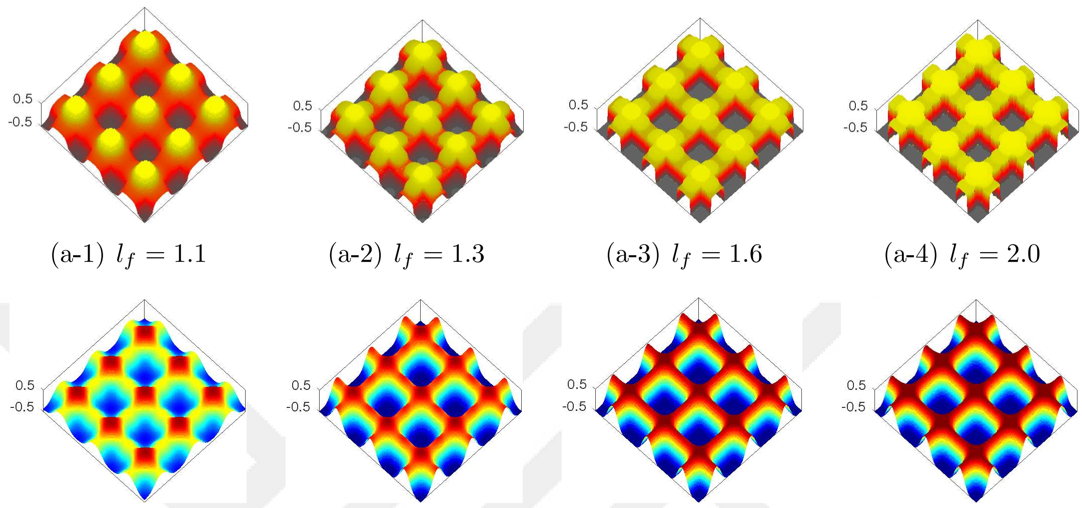

(a-1) $l_f = 1.1$ (a-2) $l_f = 1.3$ (a-3) $l_f = 1.6$ (a-4) $l_f = 2.0$

(b-1) $l_f = 1.1$ (b-2) $l_f = 1.3$ (b-3) $l_f = 1.6$ (b-4) $l_f = 2.0$

Figure 7.3: *Micro-texture optimization for prescribed load bearing capacity using (7.8). (a)* 0-OR-1 *design. (b)* 0-TO-1 *design.*

textures get thicken and the the holes get deeper for both 0-OR-1 and 0-TO-1 design, essentially due to the fact that larger load bearing capacities can only be realized by sharp micro-textures. It can also be inferred that the maximization of the load bearing capacity will give a sharp texture as well which will be verified in the following subsection.

7.1.3 Micro Texture Optimization for Maximum Load Bearing Capacity in Temporal Variations

In squeeze film flow, using velocity profile (7.1) one can divide the squeeze film cycle into time steps. In this study the squeeze film cycle is divided into 21 time steps and half of the cycle is considered, with $v_0 = -1$ is considered (i.e. when the plates are approaching each other), taking into account the fact that the calculation over the other half of the cycle is redundant. Hence, the objective can be formulated as

$$\varphi(s) = -\frac{\int_{T/2}\int_{\Omega} p_0^2(s)d\Omega dt}{\int_{T/2}\int_{\Omega} p_{ref}^2(s)d\Omega dt} \tag{7.10}$$

Here, $\int_{\Omega} p_{ref}^2 d\Omega$ is is evaluated at $h = h_0 + \bar{h}_{min}$ to scale the objective. All the other parameters are same such as minimum and maximum allowed roughness etc. Again two cases were tested for 0-OR-1 and 0-TO-1 design for a sinusoidal velocity profile $\frac{\partial h_0}{\partial t} = v_0 sin(T\pi),\ v_0 = -1,\ T = 1$ and a constant velocity profile $\frac{\partial h_0}{\partial t} = -1$. It is clear from the optimized textures (see Fig. 7.4) that maximizing the lead bearing capacity requires sharp transitions.

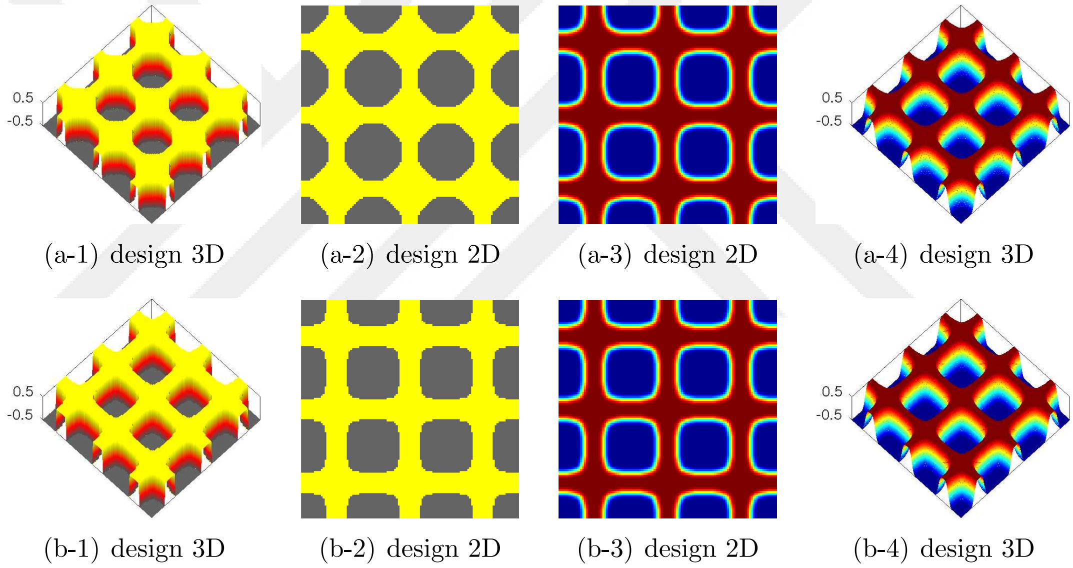

Figure 7.4: *Micro-texture optimization for maximizing the load bearing capacity (7.10). (a)* $\frac{\partial h_0}{\partial t} = v_0 sin(T\pi), v_0 = -1, T = 1$ *(b)* $\frac{\partial h_0}{\partial t} = -1$.

Using the same sets of parameters as in Subsection (7.1.2), the load factor, l_f, can be fond using (7.11) for the for optimized textures in Figure (7.4).

$$l_f = \frac{L_{opt}}{L_{hom}} \tag{7.11}$$

Here, L_{opt} is the load bearing capacity of the optimized texture. The values of l_f for maximizing the load bearing capacity in temporal variations are shown in

Table (7.1). It can be observed that the maximum allowed load bearing capacities in Subsection (7.1.2) for optimization could be $l_f \approx 2.9$ and $l_f \approx 2.3$ for 0-OR-1 and 0-TO-1 designs, respectively. Using these l_f values one could achieve even sharp textures as compared to the ones in Figure (7.3).

Table 7.1: *Load factors l_f for the optimized results for maximization of the load bearing capacity in temporal variations.*

$\frac{\partial h_0}{\partial t}$	l_f for 0-OR-1	l_f for 0-TO-1
$v_0 sin(T\pi), v_0 = -1$	2.92	2.31
-1	2.98	2.34

7.2 Wedge Problem

In fluid film bearing a positive pressure is generated by two plates moving relative to each other because there is a small angle present between them. This is known as the wedge problem (see Fig. 7.5). Again, this is a 2D problem shown in the 1D. In this study, the upper plate is smooth and moving and the lower plate is stationary and rough and at an angle with the horizontal upper plate, causing h_0 to change spatially. This spatial change in h_0 makes the problem computationally very expensive because the homogenized coefficients have to be evaluated all across the two-dimensional the lubrication interface. The homogenization theory developed in Chapter 4 is valid for the wedge problem and can be taken as it is without any change and further assumptions. Moreover the temporal change of h_0 is neglected using the stationary hydrodynamic lubrication assumption, $\frac{\partial h_0}{\partial t} = 0$. The velocity of upper plate $\boldsymbol{U}$ in (4.31) has the components $[\boldsymbol{U} cos(\theta) \quad \boldsymbol{U} sin(\theta)]$ such that when $\theta = 0$ the velocity angle of the upper plate is parallel to the angle of the wedge, which is normally changing in x-direction only. The macroscopic mean film thickness h_0 ranges from $h_{0_{min}} = 0.2$ to $h_{0_{max}} = 1.0$, unless otherwise stated. The microscopic fluid film thickness ranges from $\bar{h}_{min} = -0.2$ to $\bar{h}_{max} = 0.1$, unless stated. The presence of the horizontal velocity $\boldsymbol{U}$ activates the Couette term $\boldsymbol{C}$ and the sensitivity analysis is taken as (7.5) which is solved for each microscopic design variable s^I.

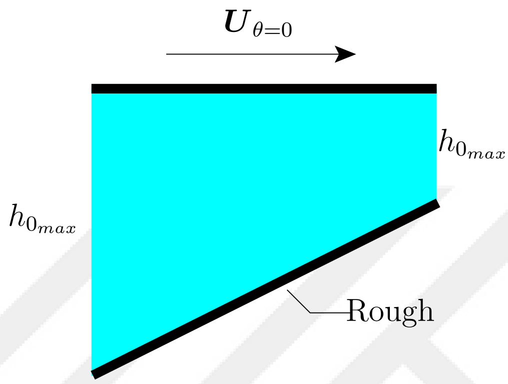

Figure 7.5: *Schematic of Wedge Problem.*

7.2.1 Micro Texture Optimization for Maximum Load Bearing Capacity in Spatial Variations

Using the numerical parameters, which are already set for MicOO and for squeeze film MacOO, the optimization problem is formulated to obtain a single texture which provides maximum load bearing capacity for the wedge. This can be done by setting the constraint for h_0 anywhere in the domain. In this study it is taken at the middle of the interface. To maximize the load bearing capacity, the following objective is employed:

$$\varphi(s) = -\frac{\int_\Omega p_0(s) d\Omega}{\int_\Omega p_{ref} d\Omega} \tag{7.12}$$

Here, $\int_{\Omega} p_{ref} d\Omega$ is the homogeneous load bearing capacity taken at $h = h_0 + \bar{h}_{min}$, which is the maximum possible value it can take without any texture. The microscopic texture optimization will again result in sharp transitions between $\bar{h}_{min}$ and $\bar{h}_{max}$ because the maximum load bearing capacity requires sharp transitions as explained earlier. Optimization at four different velocity angles ($\theta = 0\pi$, $\pi/8$, $\pi/4$ and $3\pi/8$) was conducted with filter radius $R = 8$ for 0-OR-1 design, because very small unrealizable features were observed with $R = 4$. For 0-TO-1 design choosing the filter radius more than $R = 4$ will cause delay in convergence and optimization problem will become very slow. The optimized textures show transitions in the angle of the features (dimples and holes) with the change in velocity angle (see Fig. 7.6).

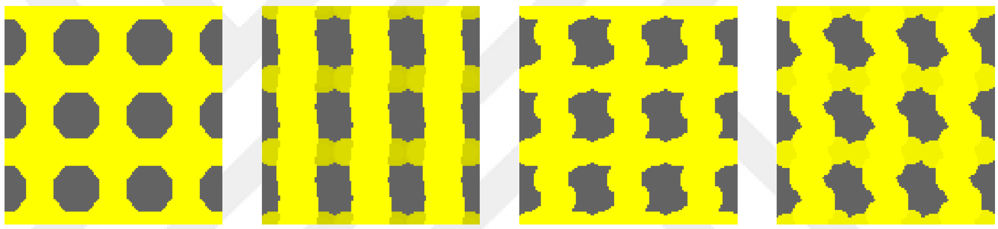

(a-1) $\theta = 0$ (a-2) $\theta = \pi/8$ (a-3) $\theta = \pi/4$ (a-4) $\theta = 3\pi/8$

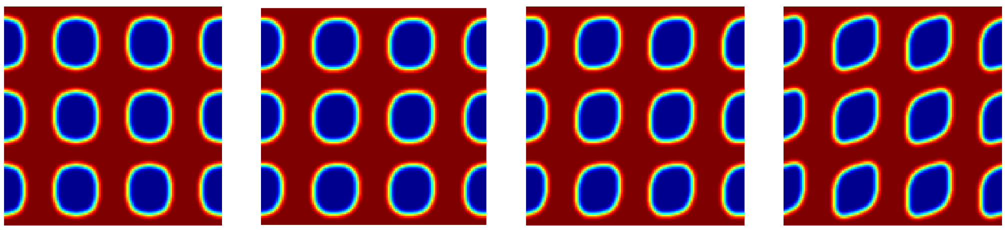

(b-1) $\theta = 0$ (b-2) $\theta = \pi/8$ (b-3) $\theta = \pi/4$ (b-4) $\theta = 3\pi/8$

Figure 7.6: *Micro-texture optimization for maximizing the load bearing capacity in spatial variations (7.12). (a)* 0-OR-1 *design with* $R = 8$ *(b)* 0-TO-1 *design with* $R = 4$.

7.3 Taylor's Approximation

Although homogenization is computationally less expensive than the direct numerical solution, in MacOO it becomes very expensive because for the default microscopic mesh resolution of $N = 40$ and macroscopic mesh resolution of $N = 20$

- $20 \times 20 \times 4 \times 4$ cell problems have to be calculated
- $20 \times 20 \times 4$ homogenized coefficients have to calculated and
- $20 \times 20 \times 4 \times 40 \times 40$ sensitivity terms (i.e., $\partial A/\partial s^I, \partial C/\partial s^I$) have to be evaluated

So, an alternative approach is sought, using Taylor's approximation the homogenized coefficients and the sensitivities are calculated at a point in the interface and approximated values are used over the interface. Buscaglia and M. Jai [53] presented the approximation as

$$\Upsilon_{T_n}(h_0) = \Upsilon(h_{0,exp}) + \sum_{i=1}^{n} \frac{1}{n!}(h_0 - h_{0,exp})^i \frac{\partial^i \Upsilon(h_{0,exp})}{\partial h_0^i} \tag{7.13}$$

Here, Υ can be replaced with the homogenized coefficients $\boldsymbol{A}$, $\boldsymbol{C}$ or their sensitivities $\partial \boldsymbol{A}/\partial s^I$, $\partial \boldsymbol{C}/\partial s^I$ to find the approximated value along the interface, n is the total number of terms in the Taylor's approximation (in this study $n = 4$) and $h_{0,exp}$ is the expansion point (it is taken in the middle of the interface). The derivatives $\partial \Upsilon(h_0, exp)/\partial h_0$ in (7.13) are calculated numerically by using 4^{th}-order central difference. Computational expense reduces from several days (approximately 1 week using 16 Cores) to several hours (approximately 8-9 hours using 8 Cores). For the optimization with Taylor's approximation everything is the same as in Subsection (7.2.1). Corresponding results to Fig. (7.6) are shown in Fig. (7.7).

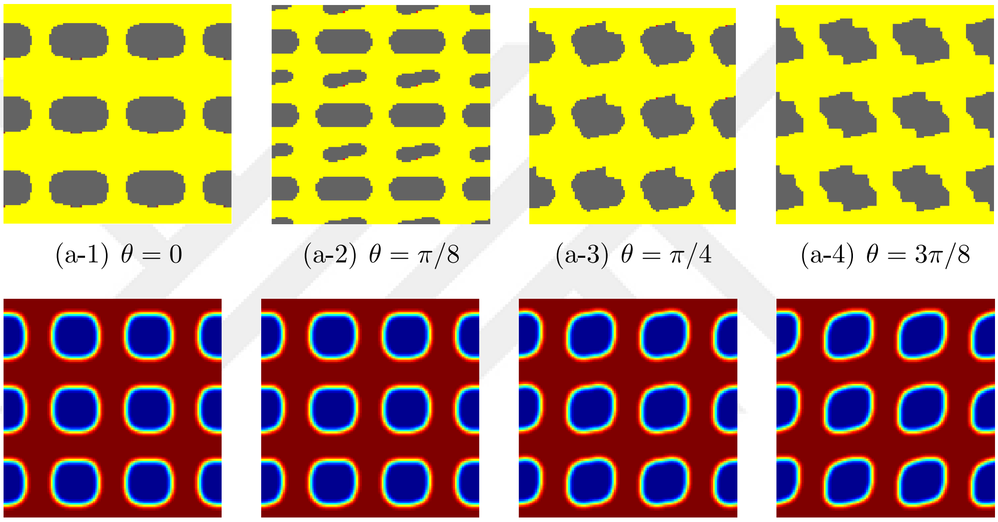

(a-1) $\theta = 0$ (a-2) $\theta = \pi/8$ (a-3) $\theta = \pi/4$ (a-4) $\theta = 3\pi/8$

(b-1) $\theta = 0$ (b-2) $\theta = \pi/8$ (b-3) $\theta = \pi/4$ (b-4) $\theta = 3\pi/8$

Figure 7.7: *Micro-texture optimization for maximizing the load bearing capacity in spatial variations with Taylor's Approximation (7.12). (a)* 0-OR-1 *design with* $R = 4$ *(b)* 0-TO-1 *design with* $R = 4$.

Chapter 8

Conclusion and Outlook

This study deals with the optimization of micro-textures for lubrication interfaces for hydrodynamic lubrication using homogenization techniques. The homogenized coefficients are designed by controlling the surface texture for a desired macroscopic response. Microscopic and macroscoic objective optimizatoins were used to check the sanity of the optimization algorithm and then both isotropic and anisotropic textures were designed for the specific input load bearing capacity, or the maximization of load bearing capacity for temporal and spatial variations. Sensitivity analysis for both micro and macro-scopic objectives were derived separately for use in the gradient-based optimization algorithm. Taylor's expansion was introduced for a comparatively less expensive optimization as compared to homogenization.

Although the present study provides a comprehensive computational framework for the micro-texture design in hydrodynamic lubrication, it has certain limitations to it. These limitations come from the basic assumption made for the use of Reynolds equation. One can only obtain the textures of the scales of the Reynolds roughness. If the roughness goes beyond this range then the Reynolds equation may not be valid anymore and one has to use the Stokes equation to solve and optimize for that roughness scale. Also the designer is limited because of the physical limitations provided by the Reynolds equation. For instance in this the multi-physics like temperature rise and viscosity change due to this temperature rise. The texture developed in this study were 2D in nature. Using Stokes or Navier-Stokes equation one might obtain non-convex 3D textures.

One can also aim for obtaining continuously varying micro-textures, which can change in shape and size smoothly from one point to another within a single lubrication interface for optimum load bearing capacity, instead of a single texture obtained in this study. This is recently done for the material optimization in [54] and thermal conductivity in [55]. Different texture endowing schemes can also be tried as well such as partial endowing at the in-flux section of the interface. Moreover, simultaneous micro-texture and macroscopic geometry optimization can be utilized for a single or multiple macroscopic objectives as done for materials in [56].

Taylor's expansion provides a computationally less expensive framework for the homogenization problems but the choice of expansion parameters requires a careful consideration. On the other hand, formulations provided by variational bounds are analytic in nature [57] and combination of upper and lower bounds for obtaining homogenized coefficients can be used for optimization, there is a limitation on bounds as well because they can only capture isotropic textures.

Many areas in engineering can take advantage of texture designing ranging from machine design to bio-mechanics. Bearings used in machines are crucial machine elements but a lot of energy is wasted during the their operation. By properly designing the interface, their life time can be significantly increased and energy consumption can also be reduced. In renewable energy sector, wind-turbine can also benefit from the surface texturing because the efficiency of the wind turbine blades can be increased by proper texturing [58].

In bio-mechanics field, surface texturing in artificial joints can also be very beneficial. With the help of surface texture it might be possible that the artificial joints can be manufactured according to patients specifications such as weight and size of the joint. This will very important for patient's overall health as well because less unwanted material will get into the patient's system because of less surface wear. Similar surface texture is valid for other implants as well, such as heart valves [59] in which soft interfaces can be taken into account [43].

Bibliography

[1] A. G. M. Michell, "The limits of economy of material in frame-structures," *The London, Edinburgh, and Dublin Philosophical Magazine and Journal of Science*, vol. 8, no. 47, pp. 589–597, 1904.

[2] K. Svanberg, "The method of moving asymptotes—a new method for structural optimization," *International journal for numerical methods in engineering*, vol. 24, no. 2, pp. 359–373, 1987.

[3] M. P. Bendsoee, "Some smear-out models for integrally stiffened plates with applications to optimal design," tech. rep., DTIC Document, 1981.

[4] M. Bendsoe, "General optimal topologies in structural design using a homogenization method," *Computer Methods in Applied Mechanics and Engineering*, vol. 93, pp. 291–318, 1988.

[5] G. Rozvany, O. Sigmund, and T. Birker, "Optimal design of composite and fibre reinforced plates," *Optimal Design with advanced materials*, vol. 23, pp. 293–309, 1993.

[6] K. Terada and N. Kikuchi, "Microstructural design of composites using the homogenization method and digital images," vol. 45, pp. 65–72, 1996.

[7] P. W. Christensen and A. Klarbring, *An introduction to structural optimization*, vol. 153. Springer Science & Business Media, 2008.

[8] M. Ohsaki, *Optimization of finite dimensional structures.* CRC Press, 2016.

[9] A. Evgrafov, K. Maute, R. Yang, and M. L. Dunn, "Topology optimization for nano-scale heat transfer," *International journal for numerical methods in engineering*, vol. 77, no. 2, p. 285, 2009.

[10] T. E. Bruns, "Topology optimization of convection-dominated, steady-state heat transfer problems," *International Journal of Heat and Mass Transfer*, vol. 50, no. 15, pp. 2859–2873, 2007.

[11] R. C. Carbonari, E. C. Silva, and G. H. Paulino, "Multi-actuated functionally graded piezoelectric micro-tools design: A multiphysics topology optimization approach," *International Journal for Numerical Methods in Engineering*, vol. 77, no. 3, pp. 301–336, 2009.

[12] C. Y. Kiyono, E. C. N. Silva, and J. Reddy, "Design of laminated piezocomposite shell transducers with arbitrary fiber orientation using topology optimization approach," *International Journal for Numerical Methods in Engineering*, vol. 90, no. 12, pp. 1452–1484, 2012.

[13] J. Park and A. Sutradhar, "A multi-resolution method for 3d multi-material topology optimization," *Computer Methods in Applied Mechanics and Engineering*, vol. 285, pp. 571–586, 2015.

[14] H.-T. C. Pedro and M. H. Kobayashi, "On a cellular division method for topology optimization," *International Journal for Numerical Methods in Engineering*, vol. 88, no. 11, pp. 1175–1197, 2011.

[15] M. Wallin, N. Ivarsson, and M. Ristinmaa, "Large strain phase-field-based multi-material topology optimization," *International Journal for Numerical Methods in Engineering*, vol. 104, no. 9, pp. 887–904, 2015.

[16] A. Clausen, N. Aage, and O. Sigmund, "Topology optimization of coated structures and material interface problems," *Computer Methods in Applied Mechanics and Engineering*, vol. 290, pp. 524–541, 2015.

[17] L. H. Olesen, F. Okkels, and H. Bruus, "A high-level programming-language implementation of topology optimization applied to steady-state navier-stokes flow," 2004.

[18] T. Borrvall and J. Petersson, "Topology optimization of fluids in stokes flow," *International journal for numerical methods in fluids*, vol. 41, no. 1, pp. 77–107, 2003.

[19] E. M. Dede, "Multiphysics topology optimization of heat transfer and fluid flow systems," 2009.

[20] L. Rayleigh, "Notes on the theory of lubrication," *The London, Edinburgh, and Dublin Philosophical Magazine and Journal of Science*, vol. 35, no. 205, pp. 1–12, 1918.

[21] C. Maday, "A bounded variable approach to the optimum slider bearing," *Journal of Tribology*, vol. 90, no. 1, pp. 240–242, 1968.

[22] C. Maday, "The maximum principle approach to the optimum one-dimensional journal bearing," *Journal of Tribology*, vol. 92, no. 3, pp. 482–487, 1970.

[23] S.-J. Yoon and D.-H. Choi, "Design optimization of the taper-flat slider positioned by a rotary actuator," *Journal of tribology*, vol. 117, no. 4, pp. 588–593, 1995.

[24] H. Hashimoto, "Optimum design of high-speed, short journal bearings by mathematical programming," *Tribology Transactions*, vol. 40, no. 2, pp. 283–293, 1997.

[25] B.-S. Yang, Y.-H. Lee, B.-K. Choi, and H.-J. Kim, "Optimum design of short journal bearings by artificial life algorithm," *Tribology International*, vol. 34, no. 7, pp. 427–435, 2001.

[26] H. Hashimoto and K. Matsumoto, "Improvement of operating characteristics of high-speed hydrodynamic journal bearings by optimum design: part i—formulation of methodology and its application to elliptical bearing design," *Journal of Tribology*, vol. 123, no. 2, pp. 305–312, 2001.

[27] H. Zhu and D. B. Bogy, "Direct algorithm and its application to slider air-bearing surface optimization," *Magnetics, IEEE Transactions on*, vol. 38, no. 5, pp. 2168–2170, 2002.

[28] S.-J. Yoon and D.-H. Choi, "Adjoint design sensitivity analysis of molecular gas film lubrication sliders," *Journal of Tribology*, vol. 125, no. 1, pp. 145–151, 2003.

[29] C.-J. Lu and T.-K. Wang, "New designs of HDD air-lubricated sliders via topology optimization," *Journal of Tribology*, vol. 126, no. 1, pp. 171–176, 2004.

[30] H. Zhu and D. B. Bogy, "Hard disc drive air bearing design: modified direct algorithm and its application to slider air bearing surface optimization," *Tribology international*, vol. 37, no. 2, pp. 193–201, 2004.

[31] S.-J. Yoon and D.-H. Choi, "Topology designs of slider air bearings," *Journal of Tribology*, vol. 126, no. 2, pp. 342–346, 2004.

[32] B. J. Hamrock, S. R. Schmid, and B. O. Jacobson, *Fundamentals of fluid film lubrication*. CRC press, 2004.

[33] A. Z. Szeri, *Fluid film lubrication: theory and design*. Cambridge University Press, 2005.

[34] G. Stachowiak and P. Podsiadlo, "3-D characterization, optimization, and classification of textured surfaces," *Tribology Letters*, vol. 32, no. 1, pp. 13–21, 2008.

[35] A. N. Murthy, M. Duwensee, and F. E. Talke, "Numerical simulation of the head/disk interface for patterned media," *Tribology letters*, vol. 38, no. 1, pp. 47–55, 2010.

[36] M. B. Dobrica, M. Fillon, M. D. Pascovici, and T. Cicone, "Optimizing surface texture for hydrodynamic lubricated contacts using a mass-conserving numerical approach," *Proceedings of the Institution of Mechanical Engineers, Part J: Journal of Engineering Tribology*, vol. 224, no. 8, pp. 737–750, 2010.

[37] M. Fesanghary and M. M. Khonsari, "On the shape optimization of self-adaptive grooves," *Tribology Transactions*, vol. 54, no. 2, pp. 256–264, 2011.

[38] A. Guzek, P. Podsiadlo, and G. W. Stachowiak, "Optimization of textured surface in 2D parallel bearings governed by the reynolds equation including cavitation and temperature," *Tribology Online*, vol. 8, no. 1, pp. 7–21, 2013.

[39] M. Scaraggi, "Optimal textures for increasing the load support in a thrust bearing pad geometry," *Tribology Letters*, vol. 53, no. 1, pp. 127–143, 2014.

[40] B. Hamrock, S. Schmid, and B. Jacobson, *Fundamentals of fluid film lubrication*. CRC Press, 2004.

[41] H. G. Elrod, "Thin-film lubrication theory for newtonian fluids with surfaces possessing striated roughness or grooving," *Journal of Lubrication Technology*, vol. 95, no. 4, pp. 484–489, 1973.

[42] T. Almqvist and R. Larsson, "Some remarks on the validity of reynolds equation in the modeling of lubricant film flows on the surface roughness scale," *Journal of tribology*, vol. 126, no. 4, pp. 703–710, 2004.

[43] G. Kabacaoğlu and İ. Temizer, "Homogenization of soft interfaces in time-dependent hydrodynamic lubrication," *Computational Mechanics*, vol. 56, no. 3, pp. 421–441, 2015.

[44] M. P. Bendsoe and O. Sigmund, *Topology optimization: theory, methods, and applications*. Springer Science & Business Media, 2013.

[45] K. Matsui and K. Terada, "Continuous approximation of material distribution for topology optimization," *International Journal for Numerical Methods in Engineering*, vol. 59, no. 14, pp. 1925–1944, 2004.

[46] S. Rahmatalla and C. Swan, "A q4/q4 continuum structural topology optimization implementation," *Structural and Multidisciplinary Optimization*, vol. 27, no. 1-2, pp. 130–135, 2004.

[47] M. Zhou, Y. Shyy, and H. Thomas, "Checkerboard and minimum member size control in topology optimization," *Structural and Multidisciplinary Optimization*, vol. 21, no. 2, pp. 152–158, 2001.

[48] K. Svanberg and H. Svärd, "Density filters for topology optimization based on the pythagorean means," *Structural and Multidisciplinary Optimization*, vol. 48, no. 5, pp. 859–875, 2013.

[49] G. I. Rozvany, "On symmetry and non-uniqueness in exact topology optimization," *Structural and Multidisciplinary Optimization*, vol. 43, no. 3, pp. 297–317, 2011.

[50] O. Sigmund and J. Petersson, "Numerical instabilities in topology optimization: a survey on procedures dealing with checkerboards, mesh-dependencies and local minima," *Structural optimization*, vol. 16, no. 1, pp. 68–75, 1998.

[51] J. K. Guest and L. C. Smith Genut, "Reducing dimensionality in topology optimization using adaptive design variable fields," *International journal for numerical methods in engineering*, vol. 81, no. 8, pp. 1019–1045, 2010.

[52] E. Sánchez-Palencia, "Non-homogeneous media and vibration theory," in *Non-homogeneous media and vibration theory*, vol. 127, 1980.

[53] G. Buscaglia and M. Jai, "Sensitivity analysis and taylor expansions in numerical homogenization problems," *Numerische Mathematik*, vol. 85, no. 1, pp. 49–75, 2000.

[54] J. Alexandersen and B. S. Lazarov, "Topology optimisation of manufacturable microstructural details without length scale separation using a spectral coarse basis preconditioner," *Computer Methods in Applied Mechanics and Engineering*, vol. 290, pp. 156–182, 2015.

[55] J. Alexandersen and B. S. Lazarov, "Tailoring macroscale response of mechanical and heat transfer systems by topology optimization of microstructural details," in *Engineering and Applied Sciences Optimization*, pp. 267–288, Springer, 2015.

[56] J. Kato, D. Yachi, K. Terada, and T. Kyoya, "Topology optimization of micro-structure for composites applying a decoupling multi-scale analysis," *Structural and Multidisciplinary Optimization*, vol. 49, no. 4, pp. 595–608, 2014.

[57] A. Almqvist, E. K. Essel, J. Fabricius, and P. Wall, "Variational bounds applied to unstationary hydrodynamic lubrication," *International Journal of Engineering Science*, vol. 46, no. 9, pp. 891–906, 2008.

[58] P. Nordin and G. Strindberg, "Wind turbine blade having an outer surface with improved properties," Jan. 14 2010. US Patent App. 13/522,349.

[59] H. Barmada, "Method for making an artificial heart valve," Aug. 22 1995. US Patent 5,443,501.

Appendix A

Basic Tensor Calculus

In Cartesian coordinate system, with coordinates x_i and orthonormal basis vector $\boldsymbol{e}_i$, a vector $\boldsymbol{v}$ can be expressed as

$$\boldsymbol{v} = v_i \boldsymbol{e}_i \tag{A.1}$$

The position vector is

$$\boldsymbol{x} = x_i \boldsymbol{e}_i \tag{A.2}$$

The gradient of a scalar quantity can be written as

$$\nabla u = \frac{\partial u}{\partial \boldsymbol{x}} = \frac{\partial u}{\partial x_i} \boldsymbol{e}_i \tag{A.3}$$

The divergence of a vector field is

$$\nabla \cdot \boldsymbol{v} = \frac{\partial v_i}{\partial x_i} \tag{A.4}$$

Here, the Euclidean inner product $\boldsymbol{a} \cdot \boldsymbol{b} = a_i b_i$ is used. Similarly,

$$\nabla \cdot [a \nabla u] = \left(\frac{\partial}{\partial x_i} \right) \left(a \frac{\partial u}{\partial x_i} \right) \tag{A.5}$$

If a is a constant,

$$\nabla \cdot [a\nabla u] = a\frac{\partial^2 u}{\partial {x_i}^2} \tag{A.6}$$

Appendix B

Target MicroTextures

Table B.1: *Benchmark* 0-OR-1 *textures with a macroscopically isotropic response — see Figure 6.6.*

Target Texture	*Gap* h_0	*Homogeneous Interface* $[A_0]$	$[C_0]$	*Heterogeneous Interface* $[A^*]$	$[C^*]$
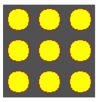	1.970	$\begin{bmatrix}4.551 & 0\\ 0 & 4.551\end{bmatrix}$	$\begin{bmatrix}0.985 & 0\\ 0 & 0.985\end{bmatrix}$	$\begin{bmatrix}6.825 & 0\\ 0 & 6.825\end{bmatrix}$	$\begin{bmatrix}0.680 & 0\\ 0 & 0.680\end{bmatrix}$
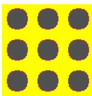	1.130	$\begin{bmatrix}0.859 & 0\\ 0 & 0.859\end{bmatrix}$	$\begin{bmatrix}0.565 & 0\\ 0 & 0.565\end{bmatrix}$	$\begin{bmatrix}0.0014 & 0\\ 0 & 0.0014\end{bmatrix}$	$\begin{bmatrix}0.0545 & 0\\ 0 & 0.0545\end{bmatrix}$
	2.239	$\begin{bmatrix}6.683 & 0\\ 0 & 6.683\end{bmatrix}$	$\begin{bmatrix}1.120 & 0\\ 0 & 1.120\end{bmatrix}$	$\begin{bmatrix}8.898 & 0\\ 0 & 8.898\end{bmatrix}$	$\begin{bmatrix}0.866 & 0\\ 0 & 0.866\end{bmatrix}$
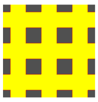	0.861	$\begin{bmatrix}0.380 & 0\\ 0 & 0.380\end{bmatrix}$	$\begin{bmatrix}0.430 & 0\\ 0 & 0.430\end{bmatrix}$	$\begin{bmatrix}0.0011 & 0\\ 0 & 0.0011\end{bmatrix}$	$\begin{bmatrix}0.054 & 0\\ 0 & 0.054\end{bmatrix}$

Table B.2: *Benchmark* 0-OR-1 *textures with a macroscopically anisotropic response — see Figure 6.7.*

Target Texture	*Gap* h_0	*Homogeneous Interface* $[A_0]$	$[C_0]$	*Heterogeneous Interface* $[A^*]$	$[C^*]$
	1.515	$\begin{bmatrix} 2.068 & 0 \\ 0 & 2.068 \end{bmatrix}$	$\begin{bmatrix} 0.757 & 0 \\ 0 & 0.757 \end{bmatrix}$	$\begin{bmatrix} 3.625 & 3.624 \\ 3.624 & 3.625 \end{bmatrix}$	$\begin{bmatrix} 0.39 & 0.33 \\ 0.33 & 0.39 \end{bmatrix}$
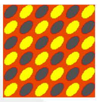	1.550	$\begin{bmatrix} 2.217 & 0 \\ 0 & 2.217 \end{bmatrix}$	$\begin{bmatrix} 0.775 & 0 \\ 0 & 0.775 \end{bmatrix}$	$\begin{bmatrix} 1.949 & 0.863 \\ 0.863 & 1.949 \end{bmatrix}$	$\begin{bmatrix} 0.446 & 0.132 \\ 0.132 & 0.446 \end{bmatrix}$
	2.062	$\begin{bmatrix} 5.215 & 0 \\ 0 & 5.215 \end{bmatrix}$	$\begin{bmatrix} 1.031 & 0 \\ 0 & 1.031 \end{bmatrix}$	$\begin{bmatrix} 7.031 & 3.338 \\ 3.338 & 5.322 \end{bmatrix}$	$\begin{bmatrix} 0.702 & 0.307 \\ 0.306 & 0.546 \end{bmatrix}$
	1.038	$\begin{bmatrix} 0.667 & 0 \\ 0 & 0.667 \end{bmatrix}$	$\begin{bmatrix} 0.520 & 0 \\ 0 & 0.520 \end{bmatrix}$	$\begin{bmatrix} 0.0027 & 0.0013 \\ 0.0013 & 0.0020 \end{bmatrix}$	$\begin{bmatrix} 0.0553 & -0.0007 \\ -0.0007 & 0.0541 \end{bmatrix}$

Table B.3: *Benchmark* 0-TO-1 *textures with a macroscopically isotropic response — see Figure 6.8.*

Target Texture	*Gap* h_0	*Homogeneous Interface* $[A_0]$	$[C_0]$	*Heterogeneous Interface* $[A^*]$	$[C^*]$
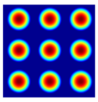	2.359	$\begin{bmatrix} 7.817 & 0 \\ 0 & 7.817 \end{bmatrix}$	$\begin{bmatrix} 1.180 & 0 \\ 0 & 1.180 \end{bmatrix}$	$\begin{bmatrix} 8.077 & 0 \\ 0 & 8.077 \end{bmatrix}$	$\begin{bmatrix} 0.955 & 0 \\ 0 & 0.955 \end{bmatrix}$
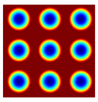	0.741	$\begin{bmatrix} 0.242 & 0 \\ 0 & 0.242 \end{bmatrix}$	$\begin{bmatrix} 0.370 & 0 \\ 0 & 0.370 \end{bmatrix}$	$\begin{bmatrix} 0.0017 & 0 \\ 0 & 0.0017 \end{bmatrix}$	$\begin{bmatrix} 0.0512 & 0 \\ 0 & 0.0512 \end{bmatrix}$
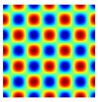	1.550	$\begin{bmatrix} 2.217 & 0 \\ 0 & 2.217 \end{bmatrix}$	$\begin{bmatrix} 0.775 & 0 \\ 0 & 0.775 \end{bmatrix}$	$\begin{bmatrix} 1.852 & 0 \\ 0 & 1.852 \end{bmatrix}$	$\begin{bmatrix} 0.558 & 0 \\ 0 & 0.558 \end{bmatrix}$
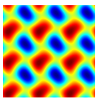	1.411	$\begin{bmatrix} 1.673 & 0 \\ 0 & 1.673 \end{bmatrix}$	$\begin{bmatrix} 0.706 & 0 \\ 0 & 0.706 \end{bmatrix}$	$\begin{bmatrix} 1.220 & 0.041 \\ 0.041 & 1.301 \end{bmatrix}$	$\begin{bmatrix} 0.469 & 0.034 \\ 0.036 & 0.458 \end{bmatrix}$

Table B.4: *Benchmark* 0-TO-1 *textures with a macroscopically anisotropic response — see Figure 6.9.*

Target Texture	Gap h_0	Homogeneous Interface $[A_0]$	$[C_0]$	Heterogeneous Interface $[A^*]$	$[C^*]$
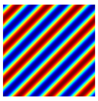	1.550	$\begin{bmatrix} 2.217 & 0 \\ 0 & 2.217 \end{bmatrix}$	$\begin{bmatrix} 0.775 & 0 \\ 0 & 0.775 \end{bmatrix}$	$\begin{bmatrix} 2.554 & 2.544 \\ 2.544 & 2.554 \end{bmatrix}$	$\begin{bmatrix} 0.423 & 0.352 \\ 0.352 & 0.423 \end{bmatrix}$
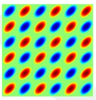	1.550	$\begin{bmatrix} 2.217 & 0 \\ 0 & 2.217 \end{bmatrix}$	$\begin{bmatrix} 0.775 & 0 \\ 0 & 0.775 \end{bmatrix}$	$\begin{bmatrix} 1.981 & 0.389 \\ 0.389 & 1.981 \end{bmatrix}$	$\begin{bmatrix} 0.620 & 0.068 \\ 0.068 & 0.620 \end{bmatrix}$
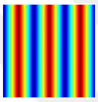	1.585	$\begin{bmatrix} 2.372 & 0 \\ 0 & 2.372 \end{bmatrix}$	$\begin{bmatrix} 0.793 & 0 \\ 0 & 0.793 \end{bmatrix}$	$\begin{bmatrix} 0.055 & 0 \\ 0 & 4.156 \end{bmatrix}$	$\begin{bmatrix} 0.122 & 0 \\ 0 & 0.775 \end{bmatrix}$
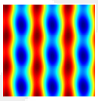	1.488	$\begin{bmatrix} 1.959 & 0 \\ 0 & 1.959 \end{bmatrix}$	$\begin{bmatrix} 0.744 & 0 \\ 0 & 0.744 \end{bmatrix}$	$\begin{bmatrix} 0.176 & 0.002 \\ 0.002 & 3.649 \end{bmatrix}$	$\begin{bmatrix} 0.210 & 0.0023 \\ 0.0042 & 0.728 \end{bmatrix}$

Table B.5: *Textures designed according to the discussion in Section 6.8 — see Figure 6.10.*

Texture	Gap h_0	Homogeneous Interface $[A_0]$	$[C_0]$	Heterogeneous Interface $[A]$	$[C]$
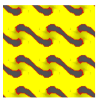	0.800	$\begin{bmatrix} 0.305 & 0 \\ 0 & 0.305 \end{bmatrix}$	$\begin{bmatrix} 0.400 & 0 \\ 0 & 0.400 \end{bmatrix}$	$\begin{bmatrix} 0.289 & -0.001 \\ -0.001 & 0.0015 \end{bmatrix}$	$\begin{bmatrix} 0.101 & 0.095 \\ 0 & 0.054 \end{bmatrix}$
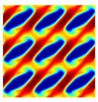	1.450	$\begin{bmatrix} 1.815 & 0 \\ 0 & 1.815 \end{bmatrix}$	$\begin{bmatrix} 0.725 & 0 \\ 0 & 0.725 \end{bmatrix}$	$\begin{bmatrix} 0.853 & 0.782 \\ 0.782 & 1.043 \end{bmatrix}$	$\begin{bmatrix} 0.304 & 0.182 \\ 0.116 & 0.397 \end{bmatrix}$